Detection and reconstruction of rock glaciers kinematics over 24 years (2000-2024) from Landsat imagery

Diego Cusicanqui[1], Pascal Lacroix[1], Xavier Bodin[2], Benjamin Aubrey Robson[3], Andreas Kääb[4] and Shelley MacDonell[5,6]

[1]Institut des Sciences de la Terre (ISTerre) CNES, CNRS, IRD, Univ. Grenoble Alpes, Grenoble, 38000, France
[2]Laboratoire EDYTEM, Univ. Savoie Mont-Blanc, Le Bourget du Lac, 73376, France
[3]Department of Earth Science, University of Bergen, Bergen, Norway
[4]Department of Geosciences, University of Oslo, Oslo, 0316, Norway
[5]Centro de Estudios Avanzados en Zonas Áridas (CEAZA), La Serena, Chile
[6]Waterways Centre, University of Canterbury and Lincoln University, Christchurch, New Zealand

Correspondence to: Diego Cusicanqui (diego.cusicanqui@univ-grenoble-alpes.fr)

Abstract. Rock glacier velocity is now widely acknowledged as an Essential Climatic Variable for permafrost. However, representing decadal regional spatiotemporal velocity patterns remains challenging due to the limited availability of high-resolution (<5 m) remote sensing data. In contrast, medium resolution satellite data (10-15 m) is globally available over several decades but has not been widely used for rock glacier kinematics. This study presents a robust methodological approach combining pairwise feature tracking image correlation with medium-resolution Landsat 7/8 optical imagery, surface displacement time-series inversion, and the automatic detection of persistent moving areas (PMA). Applied to rock glacier monitoring in the Semi-Arid Andes of South America, this methodology enables the detection and quantification of surface kinematics of 153 rock glaciers, 124 landslides and 105 unclassified landforms over 24-years across a 2250 km² area. This is the first time that Landsat images have been used to quantify rock glacier displacement time-series. The study estimates an average velocity of 0.37 ± 0.07 m yr^{-1} over 24 years for all rock glaciers, with some large rock glaciers and debris frozen landforms exhibiting surface velocities exceeding 2 m yr^{-1}. The results align well with results from high-resolution imagery, recent GNSS measurements, and previous inventories. However the L7/8 imagery-derived velocities are underestimated by approximately 20-30% in average. Additionally, high uncertainties between consecutive image pairs make it challenging to interpret annual velocity variations. Nevertheless, decadal velocity changes were observed in 2% of PMAs, where two (one) rock glaciers show a significant acceleration (deceleration) over two decades. Our calculations show that decadal velocity changes < 0.4 m yr^{-1} are associated with high uncertainty when using L7/8 data, with sensitivity depending on the reference period. Our results highlights some relations between topographic parameters as the PMA size, the orientation, slope and elevation, suggesting that permafrost thaw influences the occurrence of high-altitude landslides. This study demonstrates the feasibility of using medium-resolution optical satellite imagery for monitoring rock glacier velocity over several decades.

1 Introduction

Historically, the state of the cryosphere has been assessed using specific variables defined by Global Climate Observing System (GCOS, 1995), including mass balance for glaciers, snow cover variability and ground temperature for permafrost. Among those variables, glacier mass balance and snow cover variations are relatively well known at a global scale (Hugonnet et al., 2021; Notarnicola, 2020) compared to changes in mountain permafrost, which is still very incompletely monitored (Bolch et al., 2019).

Permafrost is an important component of the cryosphere occurring at high latitudes (i.e. polar regions) and high elevations (i.e. mountainous areas). As permafrost —ground material remaining at or below 0°C for at least two consecutive years— is a thermal phenomenon, it is thus sensitive to changes in climate forcing (Hock et al., 2019). Worldwide estimation of mountain permafrost warming relies on very few direct borehole observations (Noetzli et al., 2019), distributed mostly in the western Alps and Alaska, leaving many mountain regions without adequate monitoring data. Mountain permafrost degradation manifests by the increase in ground temperatures and active layer thickness (Etzelmüller et al., 2020), the increase of liquid water content within the frozen terrain (Cicoira et al., 2019), as well as ground-ice melt (Cusicanqui et al., 2021; Haberkorn et al., 2021). These changes also favour landslides (the downslope movement of soil, rock, and organic materials under the force of gravity). For instance, recent warming induces an increased frequency of landslides (Pei et al., 2023). However, warming affects mountain permafrost differently according to the type of terrain, particularly due to the snow cover influence. Steep rock slopes, where snow is scarce, exhibit a steady warming trend (Magnin et al., 2024), whereas loose rock formations such as rock glaciers show pronounced inter-annual variations, mostly due to the variable insulating effect of snow (Thibert & Bodin, 2022; Kellerer-Pirklbauer et al., 2024).

In the present paper, we follow the definitions proposed by the IPA Rock Glaciers Inventory and Kinematics (RGIK) action group, stating that rock glaciers can be defined as “debris landforms generated by the former or current creep of frozen ground (permafrost), detectable in the landscape with the following morphologies: front, lateral margins and optionally ridge-and-furrow surface topography” (Berthling, 2011; RGIK, 2023). Given the complexity of measuring permafrost warming, rock glacier velocity has been recently proposed and accepted by the GCOS to be a complement of the Essential Climatic Variable (ECV) permafrost (Hu et al., 2025). The thermally-dependent creep of ice-rich frozen ground is inherently sensitive to climatic conditions and fluctuates over different timescales (Delaloye et al., 2010; Kääb et al., 2007; Sorg et al., 2015). Inter-annual, seasonal and short-term variations in creep velocity primarily reflect weather influences (Kenner et al., 2017; Wirz et al., 2016), while long-term trends— decadal to pluri-decadal—correlate with mean annual air or ground temperatures (Pellet et al., 2022, Kellerer-Pirklbauer et al., 2024).

Since the early 2000s, there has been a growing interest from the international community in monitoring rock glacier velocities. Observations indicate that rock glacier velocities often exhibit similar interannual to long-term trends at a regional scale (Kellerer-Pirklbauer & Kaufmann, 2022; Marcer et al., 2021; Pellet et al., 2022), largely driven by local ground temperature changes (Noetzli et al., 2019). Velocity of rock glaciers is controlled by the landform's intrinsic characteristics, particularly its internal structure (ice / debris proportions, thickness) and the topography (bed slope), while external climatic factors—such as ground temperature, advection, infiltration, and internal meltwater production—also play a significant role (Jansen and Hergarten, 2006; Cicoira et al., 2019; Kenner et al., 2020). Thus, the magnitude and variability of their velocity can give an indication on their current state and possible ongoing changes in the characteristics of the permafrost body. As a consequence, monitoring rock glacier velocity changes provides information about the impact of climate change on mountain permafrost, indirectly, on its thermal state. Given the observed current warming context of mountain permafrost (Noetzli et al., 2019), the velocity of rock glaciers in cold mountains is expected to increase with ground temperature (Arenson et al., 2015; Kääb et al., 2007; Müller et al., 2016).

Quantifying rock glacier velocity at regional scales has been first achieved using satellite radar interferometry (InSAR) data. This method enables the detection of slow slope movement (i.e. rock glacier motion) in the satellite's Line of Sight (LOS) across large regions and hundreds of individual landforms (Hu et al., 2023). This approach has been used to map rock glacier motion around the world (Bertone et al., 2022). This data source has served as a base for classifying movement rates of various orders of magnitude (cm/d, cm/month, dm/month, cm/a, etc.), recently standardised within the RGIK group (RGIK, 2023). However, even if this technique is well suited for rock glacier mapping (Barboux et al., 2014), it is most effective for relatively slow rock glacier speeds, with maximum detectable speed of approximately 1–1.5 m yr^{-1} over short observation periods (6, 12 days). Beyond this threshold, InSAR signals become geometrically decorrelated and thus uninterpretable (Villarroel et al., 2018). In addition, freely available high-temporal-resolution SAR data has only been accessible since the early 21st-century (Strozzi et al., 2020), preventing the assessment of climatic timescales (i.e. decadal trends) for rock glaciers velocity.

Comparatively, feature-tracking applied to repeat and historical optical imagery offers a more robust alternative to derive rock glacier surface displacements and velocity, over extended timescales (Cusicanqui et al., 2021; Kääb et al., 2021; Kaufmann et al., 2021). This technique is less suitable for slow velocities due to a low signal-to-noise ratio (unless very high spatial resolution allows tracking the movement), but is well suited for medium to large movements beyond 1 - 1.5 m yr^{-1} (Hartl, et al., 2023; Marcer et al., 2021). To date, applications have been limited to high resolution optical imagery (<5 m), often requiring airborne imagery that is prohibitively expensive for larger regions or for more extensive time series. As a consequence, few periglacial regions have been extensively investigated using feature tracking, with a research focus on the European Alps (Cusicanqui et al., 2021; Hartl et al., 2016; Kellerer-Pirklbauer and Kaufmann, 2012), some isolated regions

in the Andes (Vivero et al., 2021; Blöthe et al., 2021), in northern Tien Shan (Kääb et al., 2021; Wood et al., 2025) and more recently, the United States (Kääb and Røste, 2024).

Medium-resolution imagery (Landsat-4/5/7/8, SPOT 1-4, ASTER) has provided continuous data for monitoring slow-moving landforms since the 1980's. Recent progress in time-series processing has enabled the development of methods for both detecting and monitoring slow-moving landslides using medium-resolution imagery over the last 40-50 years (Bontemps et al., 2018; Lacroix et al., 2020a). However, these methods have never been applied to rock glaciers due to their slow motions (~ 1 m yr^{-1}) and the challenges posed by the presence of snow and shadows in steep mountains. Here, we demonstrate the applicability of the free and open-access, global, medium-resolution satellite datasets Landsat 7/8 (called hereafter L7/8) to characterise rock glacier displacements and velocities for the early 21th century in a region of the semiarid Andes (both on Chile and Argentina). We further validate our results at a regional scale using Sentinel-1 wrapped interferograms, and at a local scale with very high resolution (called hereafter VHR) datasets e.g. Geoeye, Pléiades, airborne on the Tapado complex area and recent Global Navigation Satellite System (GNSS) measurements.

2 Study area and previous work

Our study area lies within the Coquimbo and San Juan provinces, in the semiarid Andes of Chile and Argentina (29°20'S-31°15'S; Fig. 1). It covers ~45x45 km², with altitudes ranging from 3,000 to 6,300 m above sea level (a.s.l). The regional climate is characterised by semi-arid conditions, influenced mainly by the subtropical South Pacific anticyclone (Montecinos & Aceituno, 2003). The rugged topography from coastal locations to the high-elevation of the Andes mountain range (~6,000 m.a.s.l.) strongly affects atmospheric circulation, differentiating the eastern and western climatic regimes (Kalthoff et al., 2002). Schauwecker (2022) shows that precipitation from humid Pacific air masses occurs almost exclusively as snowfall, concentrated in the austral winter (May-August). Year-to-year precipitation varies notably in accordance with the El Niño Southern Oscillation (ENSO) phenomenon with above (below) -average precipitation during El Niño (La Niña) events (Masiokas et al., 2006, 2010) with recent deficits in precipitations between 20-40% (Garreaud et al., 2020). Meteorological records by three Automatic Weather Stations (AWS) show mean annual precipitation of ~170 mm in the last decade (CEAZA, 2023). Recent air temperature studies show a warming trend of 0.2°C per decade in the central Andes, contributing to decreasing snowfall (Poblete & Minetti, 2017; Réveillet et al., 2020).

According to global permafrost distribution models (Gruber, 2012; Obu, 2021) and a local one (Azócar et al., 2017), heterogeneous/discontinuous permafrost occurs between 3,900 - 4,500 m a.s.l., becoming widespread above 4,500 m a.s.l. (Fig. 1). Several rock glacier inventories exists for the Chilean (DGA, 2022) and Argentinian (IANIGLA, 2018) Andes, alongside detailed/local geomorphological investigations (Monnier & Kinnard, 2015, 2016, Halla et al., 2021; Navarro et al., 2023a; de Pasquale et al., 2022). According to both inventories of Chile and Argentina (both based on geomorphological

interpretation of optical satellite imagery) the area has a relatively high number of rock glaciers with 80 located on the Chilean side and 235 on the Argentinian side (Fig. 1). The study of mountain permafrost in this region of the semi-arid Andes has received attention during the last decades because of the high density and large extension of rock glaciers (Janke et al., 2015). Recent studies highlight the complex interaction between remnants of glaciers, debris covered glaciers and rock glaciers (Navarro et al., 2023b; Robson et al., 2021) as well as the role of rock glaciers as water storage resources (Azocar and Brenning, 2010; MacDonell et al., 2022; Schaffer et al., 2019; Schaffer and MacDonell, 2022).

Despite growing interest, limited information is available on rock glacier velocities, and historical velocity trends. Villarroel et al. (2018) provided a kinematic inventory of the Argentinean Andes (30.5°S–33.5°S), identifying ~2100 active rock glaciers using InSAR. On the other hand, Blöthe et al (2021) provided a regional assessment in the "Cordon del Plata" range (~300 km south of our study area), quantifying velocity fields of 244 rock glaciers between 2010 and 2017/18 using offset tracking between optical imagery. Only two rock glaciers in this region are monitored i.e. Dos Lenguas rock glacier studied primarily with InSAR (Strozzi et al., 2020) and more recently with Uncrewed Aerial Vehicle (UAV; Stammler et al., 2024) in Argentina and the Tapado complex in Chile (Vivero et al., 2021), monitored since 2009 using GNSS and historical aerial images, providing the longest surface velocity time series since the 1950's. In this sense, a historical perspective on velocity trends remains largely absent in this region. Finally, this region was chosen due to good coverage of reference datasets, namely VHR satellite imagery and in situ GNSS measurements on the Tapado rock glacier (DGA, 2010), which serve as validation sources.

5

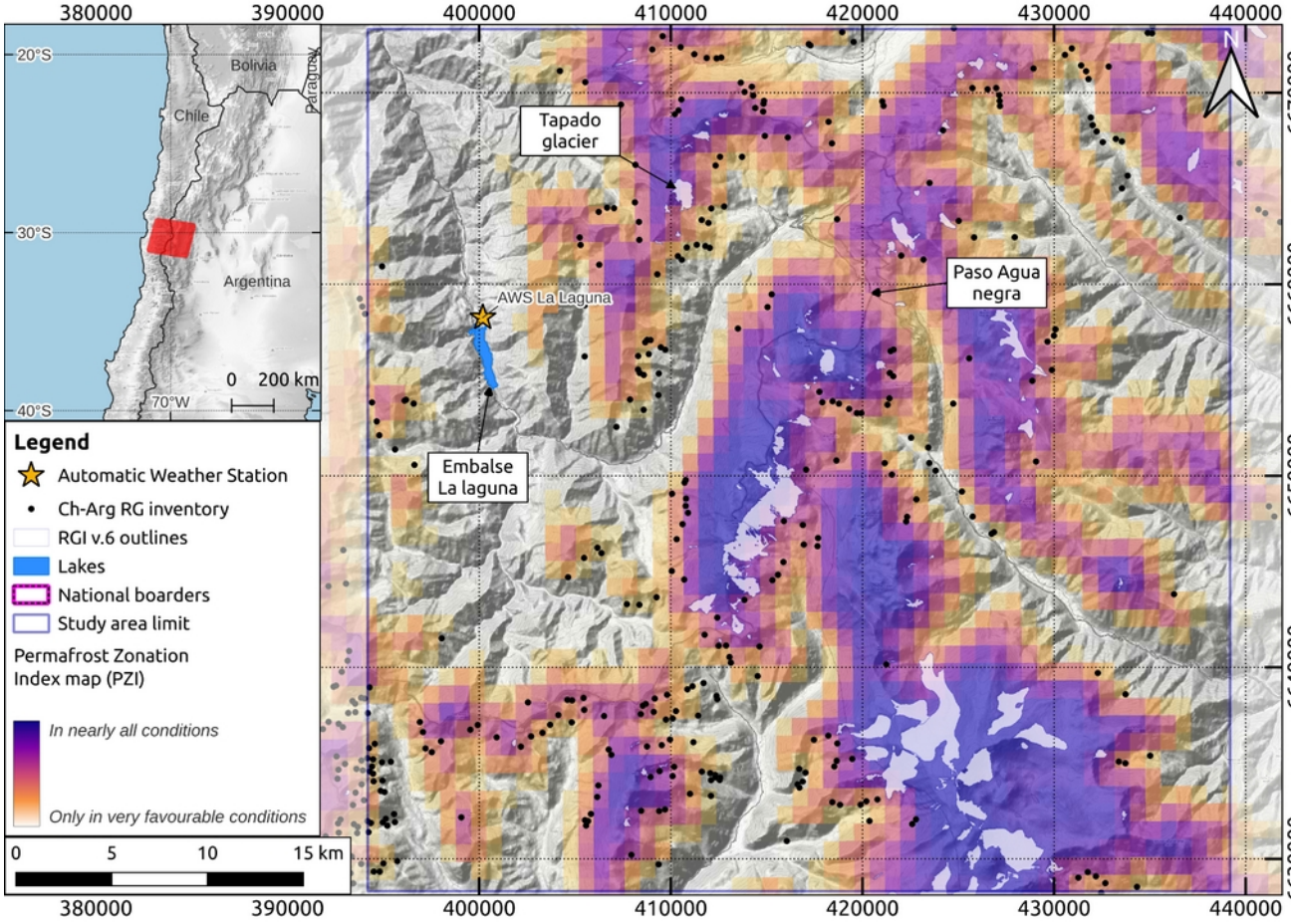

147 **Figure 1:** Location of the study area in the semiarid Andes (29°20'S-31°15'S). The red square in the inner map shows the
148 footprint of the Landsat scenes used in this study. Within the main map, black dots correspond to rock glacier inventory for
149 Chile (DGA, 2022) and Argentina (IANIGLA, 2018). The orange-purple colorbar represents the Permafrost Favorability
150 Index (PFI) from (Gruber, 2012). A comparison with the more recent PFI from Obu (2021) is shown in Fig. S1. Background
151 map corresponds to © OpenTopoMap.

152 **3 Data**

153 Three different remote sensing datasets were used in this study: *(i)* L7/8 images, *(ii)* VHR images from airborne platforms
154 and satellites, used to validate the L7/8 products temporally, and *(iii)* Sentinel-1 SAR interferograms, used to validate the
155 L7/8 products spatially. Additionally, GNSS data from a specific rock glacier was used for kinematic validation.

6

3.1 L7/8 dataset

The L7/8 dataset comprises freely available 8-band multispectral orthorectified satellite images spanning 2000-2024 period (Fig. 2a and b). Only the panchromatic band (B8) was used, with the highest spatial resolution (15 m). Due to the Scan Line Corrector failure on the Landsat-7 satellite (2004-2013;Markham et al., 2004), scenes from this period were excluded to avoid data gaps. All images correspond to path/row 233/081.They were cropped to a common grid (3001x3001 pixels) covering 45x45 km². One image per year was visually selected during the summer months (January to -April) to avoid snow and cloud cover (Table S1).

3.2 VHR dataset

The VHR dataset comprises high-resolution satellite orthoimages acquired at irregular intervals between 2000 and 2020 (Fig. 2b). These images comprise data from three different sensors; aerial (0.5 m), Geoeye (0.5 m) and Pleiades (0.7 m). In this dataset, the panchromatic image bands were orthorectified and resampled within the same grid with a spatial resolution of 1x1 m. Given the variable spatial coverage of the VHR datasets, two sub-areas (i.e. Tapado and Largo RG sub-regions, respectively; Fig. 2) were selected to assure a temporal coverage comparable to the L7/8 dataset.

Most of the VHR images were already orthorectified and used directly by Robson et al., (2022), except for: *(i)* the photogrammetric flight in 2000's and *(ii)* the 2014 Pleiades acquisition. Regarding the 2000's photogrammetric flight, data were reprocessed to extend coverage to the Largo rock glacier (4 km north from Tapado complex area; Fig. 2d) initially omitted in Robson et al., (2022). The photogrammetric processing was based on the method set out by Cusicanqui et al., (2021) using Agisoft Metashape software v. 2.0.3 (Smith, 2011). Sixteen Ground Control Points (GCPs) were used across both sub-areas, with the 2019 Pleiades DEM serving as a reference for the GCPs (Robson et al., 2022). A coregistration step, based on Nuth & Kääb (2011), corrected small shifts in the 2000's aerial DEM.

For the 2014 Pléiades acquisition, processing followed Cusicanqui et al., (2023) to process the stereo pair without GCP's, using only Rational Polynomial Coefficients (RPC). The 2014 stereo DEM was subsequently coregistered to the 2019 Pléiades DEM, and orthoimages were adjusted accordingly. Finally, VHR images were acquired during the dry season (November- to April) over almost two decades (Table S1).

7

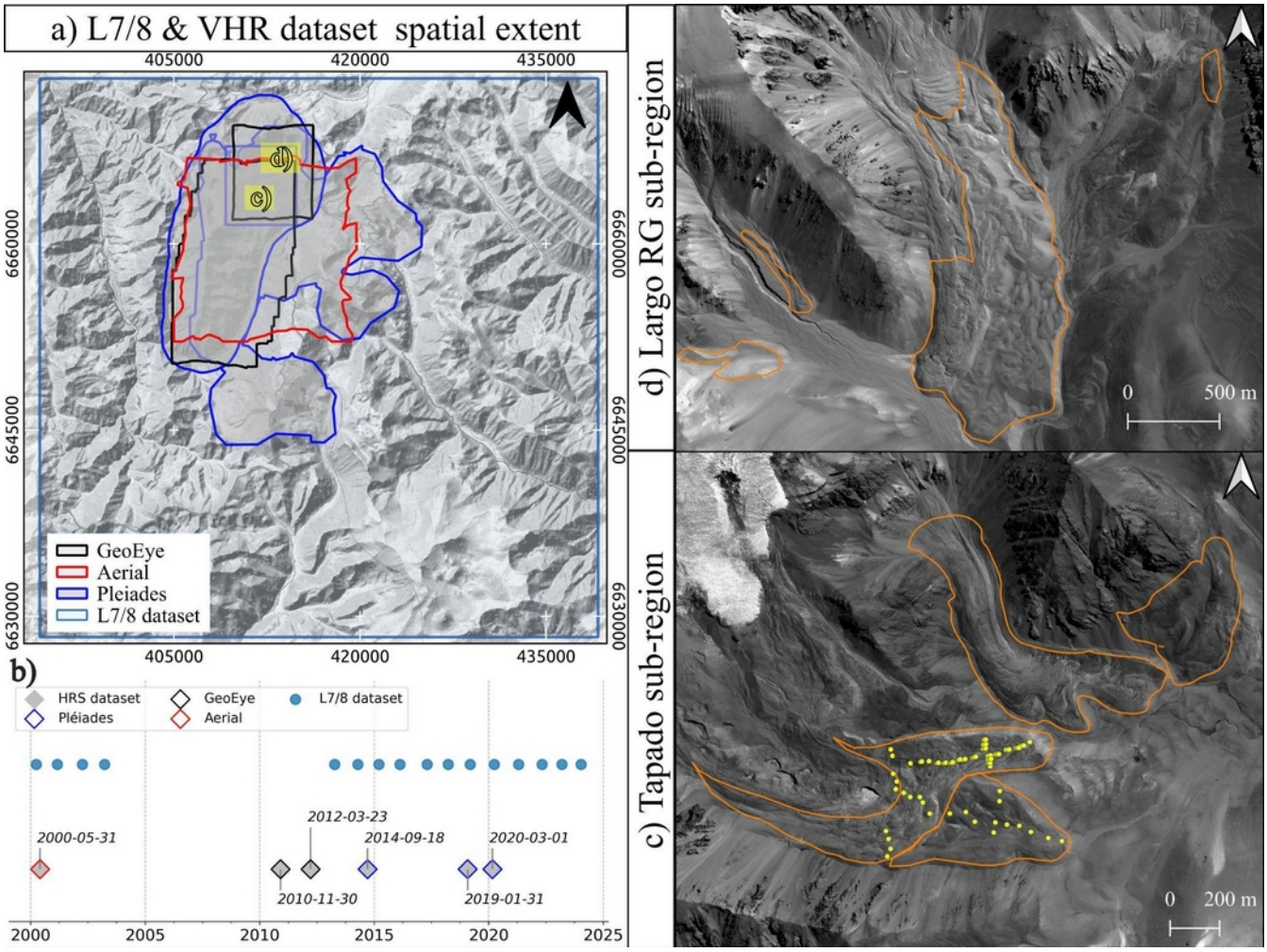

Figure 2: a) and b) Spatial extent and temporal distribution of L7/8 and VHR datasets, respectively; c) and d) Zoom over high resolution sub-regions used for validation. Orange polygons represent the 2013 rock glacier inventory from DGA, (2010) and yellow-dots represent the GNSS network on the Tapado complex (CEAZA, 2023). Image backgrounds correspond to © OpenTopoMap for a) and Pléiades 2019 imagery © CNES/AIRBUS for c) and d).

3.3 Sentinel-1 interferograms

Due to the limited spatial extent of the VHR dataset, we used raw Sentinel-1 wrapped interferograms to validate the classification of the L7/8 surface displacement products (cf. Section 4.3). This analysis involved visual inspection of multiple interferograms covering the entire study area. Sentinel-1 interferograms were processed using the ForM@Ter LArge-scale multi-Temporal Sentinel-1 InterferoMetry processing chain —FLATSIM— service (Thollard et al., 2021) at different temporal baselines (12, 60 and 360 days). This study utilized 40 interferograms from early winter 2022 to late winter 2023 in both ascending and descending orbits (paths 120 and 156, respectively; Table S2). These interferograms were

8

averaged in 2-looks (2 pixels in azimuth, 8 pixels in range) in radar geometry, equivalent to about 30 m in terrain geometry. In brief, FLATSIM service systematically produces interferograms from Sentinel-1 data and displacement time series, over large geographical areas. This service is based on the InSAR "New Small temporal and spatial BASelines" (NSBAS) processing chain as described in Doin et al., (2011) and Grandin (2015). FLATSIM products were corrected topographically using a SRTM-DEM and atmospherically corrected using ERA-5 atmospheric model mapped on the DEM. Full details can be found in Thollard et al., (2021) and ForM@TER platform.

3.4 GNSS data

The surface kinematics of the Tapado rock glacier have been measured since 2009 over 61 points (DGA, 2010) by the Centro de Estudios Avanzados en Zonas Áridas (CEAZA), using a differential GNSS (dGNSS). According to CEAZA (2012, 2016) and Vivero et al. (2021), the base station coordinates were fixed using the Trimble CenterPoint RTX post processing service, while differential GNSS data were processed with Trimble Business Center software (TBC, V.4). The reported average horizontal and vertical precisions (95%) were 0.02 and 0.04 m, respectively. To address inconsistencies in point locations i.e. points systematically shifted by few metres in north-east direction, 14 points corresponding to the same block and specific dates (2013-12-11, 2022-04-06, 2010-12-06) were removed. The remaining dataset comprises 47 points and was primarily used to validate surface velocity maps derived from both L7/8 and VHR dataset (cf. Section 5.3). Additionally, as no GCPs exist for Largo rock glacier, 13 pseudo-GCPs were manually tracked on representative features clearly identified on the VHR dataset to compare with L7/8 dataset (cf. Section 5.3).

4 Methods

Our methodology relies on the feature-tracking image correlation strategy, analyzing a large number of images available for the site. Subsequently, time-series inversion techniques were applied to the correlated images to derive consistent surface displacement fields over time (Section 4.1). Then, a medium-resolution DEM was used to identify Persistent Moving Areas (PMAs) along the slope direction (Section 4.2). Finally, we validate the final surface velocity fields by comparing them to recent dGNSS measurements and feature tracking of both L7/8 & VHR datasets in two small sub-regions in the upper La Laguna catchment (i.e. Tapado region).

4.1 Inversion of displacement time-series

Horizontal displacement time series were derived from L7/8 and VHR orthorectified images, following a similar approach developed in Bontemps et al., (2018), classically applied on slow moving landslides (e.g. Lacroix et al., 2019). The method used in this study is summarized as follows:

a) Feature tracking image correlation was performed in all possible pairwise combinations and their permutations (i.e. forward and backward). Two different software were used. Firstly, we used Mic-Mac (Rupnik et al., 2017) through

the Normalised Cross Correlation (NCC) algorithm to correlate images within the L7/8 dataset. This software was selected for its ability to handle images with low radiometric contrast and for small objects (Lacroix et al., 2020a). Secondly, the Ames Stereo Pipeline (ASP) (Beyer et al., 2018) was employed to correlate image pairs within the VHR dataset. In ASP, the More Global Matching (MGM) implementation (Facciolo et al., 2015) was used to perform image correlation. The MGM algorithm reduces high-frequency spatial artefacts (compared to classic NCC algorithms) in textureless regions and produces smooth surface displacement fields. Image mismatches associated with georeferencing errors are minimised due to the pre-alignment strategy (i.e. automatic identification of image features matched in a pair of images used then as tie-points) before the feature tracking stage. Both softwares present an adaptive windows matching strategy corresponding to 3x3 for MicMac and 7x7 for ASP as the smallest window size.

b) In both cases, all pixels with low correlation coefficient values (CC < 0.6) and displacement magnitudes > 120 m, were masked. Furthermore, an additional glacier outline masking step was applied to the VHR dataset, to avoid noisy displacement values due to glacier retreat. The Randolph Glacier Inventory (RGI v.6) was used as the source of glacier outlines (RGI Consortium, 2017).

c) Additionally, the median surface displacement value was subtracted from the both east-west (EW) and north-south (NS) displacement maps for all pairs.

d) For the L7/8 dataset, striping effects from sensor inter-band misalignments (Ayoub et al., 2008; Leprince et al., 2008) were mitigated by subtracting the median value of the stacked profile in the along-stripe direction, considering only stable areas (cf. Section 4.3).

e) A least-square inversion was applied to the redundant displacement pairs for each pixel, separately for EW and NS components (Bontemps et al., 2018). This process reduced uncertainties by approximately 30%, as shown in prior applications on SPOT 1-4 images. A weight strategy can be added to the different pairs during the inversion, to take into account the surface-cover changes over time. Due to the arid and natural cover of our area of study, this weight is not used here.

4.2 Automatic extraction of PMAs

The cumulative surface displacement time-series from L7/8 images were used to automatically extract PMAs. PMAs consist of connected pixels displaying coherent movement over time and following the downslope direction, as expected for gravity-driven processes (e.g; rock glaciers, landslides) or erosional processes (e.g. shifting rivers, river bank erosion). This methodology, developed by Dehecq et al., (2015), proposes to use the direction coherence of the displacement (called the vector coherence) with time to detect active pixels. A TanDEM-X World DEM with 12 m resolution, smoothed with a 7x7 median filter (approximately 90 m) was used to compute the slope orientation and identify pixels consistent with gravitational movements. Pixels with mean velocity vectors deviating by more than 45° from the downslope direction (calculated over a 200m kernel size) were removed to account for large-scale topographic undulations. These higher

parameter thresholds were selected after multiple trials, considering the lower resolution of the images used compared to Stumpf et al., (2017), and the presence of snow in high mountains that can alter the quality of the displacement fields. Following this pixel-based approach, isolated pixels were removed.

4.3 PMA characterisation using InSAR and high resolution imagery

As mentioned in Section 3.3, InSAR wrapped interferograms were used mainly for validation and characterization of automatic PMA detection. Rather than create a new inventory of moving areas, we manually checked all polygons resulting from PMA methodology (cf. Section 4.2) against the interferograms. Following Barboux et al. (2014) and RGIK (2023), a combination of all available interferograms (Table S2) with high resolution Google Earth imagery was used to classify PMAs. A PMA was considered 'confirmed' if its polygon overlapped a clear InSAR fringe pattern at any interval (12, 60 and 360 days; Fig. 3). The final classification consisted of two categories: 'confirmed' and 'not confirmed'. Additionally, a simple geomorphological class based on high resolution Google Earth imagery was assigned to each polygon. The geomorphological class reflects the landform overlapping the PMA. For instance, a landslide class was assigned when cracks and scarps were present at the surface. Rock glacier class was assigned when typical morphology (i.e. front and lateral margins with ridge-and-furrow surface topography) was observed. When no clear interpretation about the movement and geomorphic interpretation could be assessed on either InSAR or Google-Earth basemaps, the 'unclassified' class was assigned to those PMA. These features were often near ridges or valley bottoms (i.e. river banks erosion, road construction, …). Finally, a velocity class to each PMA was assigned based on RGIK (2023) recommendations (cf. Section 6.2).

11

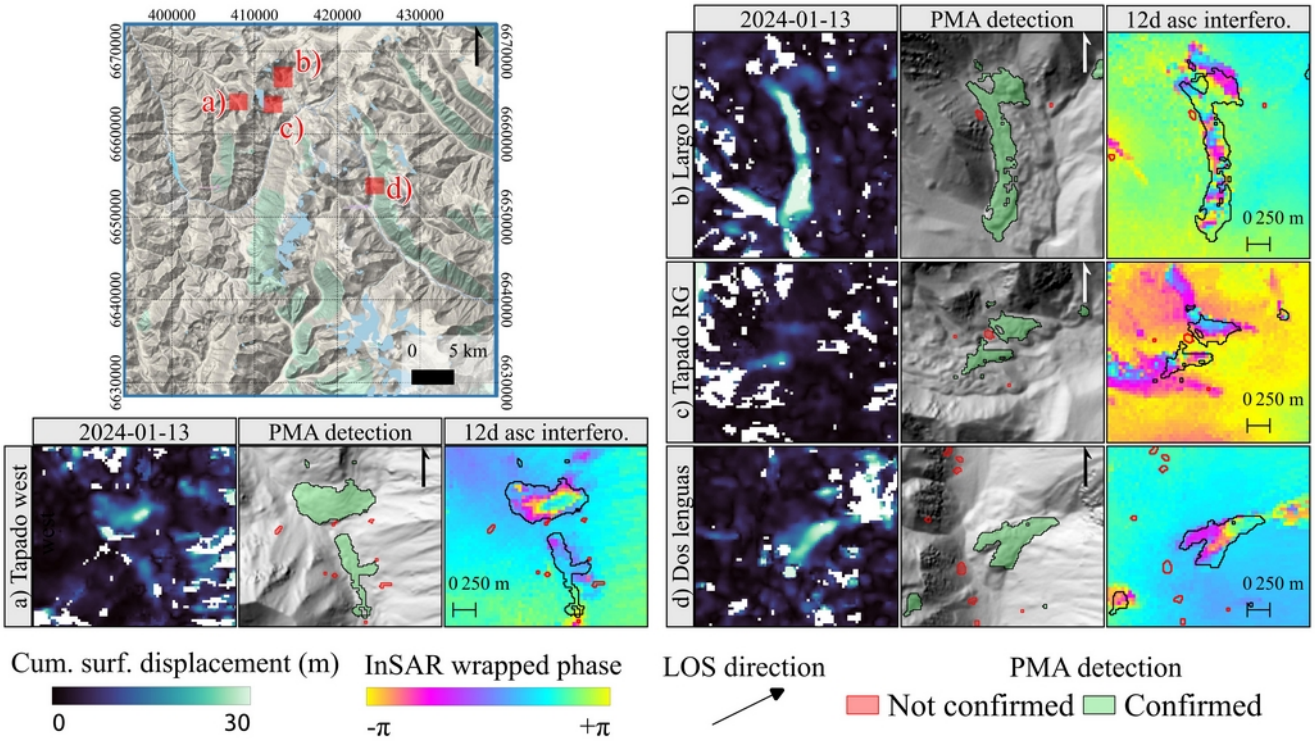

274 **Figure 3:** Example of raw outputs from inversion time-series, PMAs detection, and PMAs validation using InSAR wrapped
275 interferograms. Upper left map shows the location of small inner maps a) Tapado west, b) Largo RG, c) Tapado complex
276 and d) Dos Lenguas. Image background corresponds to © GoogleTerrain. All inner maps show cumulative surface
277 displacement map (left) after inversion time-series (last date available),PMA's detection after directional and magnitude
278 filtering (middle) and 12 days ascending S1 wrapped interferograms (right). Red and green polygons represent raw 'non
279 confirmed' and 'confirmed' PMAs, respectively.

280 **4.4 Average spatial velocity and relative velocity changes**

281 The average velocity fields were estimated using a linear fit of the cumulative surface displacements per pixel though time.
282 The representative surface velocity was extracted for each confirmed PMA. The most common approach to obtain average
283 representative surface velocity values is to use the most active portion, typically near the central profile (RGIK, 2023). This
284 avoids the potential for lateral variability within the landform (Fig. 3). For instance, Kääb et al., (2021) selected small active
285 sectors to represent the overall velocity of an entire rock glacier. Nevertheless, defining this 'active' area remains somewhat
286 subjective and may vary between users. Alternatively, Blöthe et al., (2020) proposed selecting pixels at the 95th percentile
287 above the limit of detection (LoD) to reduce lateral effects. As shown in Fig. 3a to d, the pixels located in the borders often
288 have values close to 0 m yr-1, due mainly to natural behaviour of rock glaciers—increased friction and low/no ice content in
289 lateral margins—as well as to window sizes of feature-tracking algorithms. So, the boundary effect for each PMA can bias

the average velocity. To mitigate this bias, we propose a similar approach to Blöthe et al., (2020), retaining only the Top 50% of pixels within each PMA (hereafter referred to as Top 50% average velocity) to better represent spatial velocity (cf. Section 6.3).

Uncertainties of surface displacement and velocity fields were computed using the Normalised Mean Absolute Deviation (NMAD; Höhle and Höhle, 2009) over stable areas, defined using TanDEM-X DEM and slopes below 35°. Glacier outlines from RGI consortium (2017) and surroundings (with a 500 m buffer) and all PMAs—both confirmed and unconfirmed—were excluded. Stable areas account for 53% of the study area (i.e.45x45 km²; Fig. S4).

In this study, relative velocity changes between two periods are considered and can be calculated using Equation 1, by using the first period as the reference. The related uncertainties of the relative velocity change can be calculated using Equation 2, assuming that the NMAD for both periods is similar and not correlated (σV; cf. Section 5.4). Finally, from Eq. 1 and Eq. 2 we estimate a pixel-based relative velocity change and their related uncertainty, for each PMA.

$$V_{change} = \frac{V_2 - V_1}{V_1} \quad (1)$$

$$\sigma V_{change} = \sigma V \frac{\sqrt{V_1^2 + V_2^2}}{V_1^2}, \quad (2)$$

5 Results

5.1 Characterization of PMA extraction

Within the L7/8 dataset coverage area, the automatic PMA detection produced 1710 polygons of moving objects. Raw PMAs area ranges from 225 to ~755,000 m² (Fig. 4). All PMAs were verified using InSAR and optical cross-check validation (cf. Section 4.3). From this analysis, 29% of PMAs were classified as 'confirmed' (n = 501). Among these, 42% were identified as rock glaciers, 32% as landslides and 26% polygons as 'unclassified'. Among the rock glacier class, we identified six rock glaciers directly connected to a debris-covered glacier. These remained in the 'rock glacier' class rather than creating a separate category, as PMA coverage was predominantly over the rock glacier component. Table 1 summarises all features and classes identified through the interpretation analysis. Conversely, 71% of PMAs (n = 1209) were classified as 'not confirmed' due to a lack of clear interpretation from Google Earth optical imagery and interferograms. Among the 'not confirmed' PMAs, 10% (n = 116) corresponds to glacier class and were directly removed from the dataset. Table 1 summarises all features and classes identified through the interpretation analysis.

Table 1: Summary of raw PMA geomorphological characterisation through cross-check verification using S1 InSAR and Google Earth optical imagery (cf. Section 4.3). Information about their statistical distribution is presented in Figure S1.

TOTAL POLYGONS		Manual characterization		Above automatic surface threshold (2250 m² - 10 pixels)	
		n	%	n	%
Confirmation class	Geomoph class	1710	100	975	100
NOT CONFIRMED by InSAR	Sub total	1209	71	593	61
	unclassified	747	62	382	64
	valley bottom	159	13	77	13
	ridges	155	13	79	13
	landslide	17	1	14	2
	rock glacier	15	1	5	1
	glaciers	116	10	77	13
CONFIRMED by InSAR	Sub total	501	29	382	39
	rock glacier	211	42	153	40
	landslide	160	32	105	27
	unclassified	130	26	124	32

During the manual characterization process, we noticed the presence of an important number of small and isolated polygons within the 'not confirmed' class (Fig. 4), mostly near mountain ridges and valley bottom (Fig. S3). As these tiny polygons could not be correctly interpreted, a surface threshold of 2250 m² (i.e. 10 pixels) was applied to remove them automatically. This threshold was selected based on the PMA size and the corresponding InSAR fringe pattern (cf. Section 3.3; Fig. 3), as interpretation became difficult below this threshold. Applying this threshold, 43% (n = 735) of all PMAs were removed from the analysis.

The selected surface threshold effectively removed noisy (smaller) PMAs while retaining coherent (larger) PMAs, by only compromising 15% of confirmed PMAs (Fig. 4). After applying a surface threshold and removing PMAs classified as glaciers, the remaining filtered dataset contains 901 PMAs (47% of the initial dataset), of which 39% (n = 382) of PMA are confirmed. These confirmed PMAs correspond to rock glaciers and mostly large landslides (Tab. 1),with a mean surface area of ~30,000 m² (Fig. S3). The remaining 61% (n = 519) of not confirmed PMA also represent a consistent group of pixels, potentially representing landslides, but could not be validated through cross-check methodology (cf. Section 4.3). These unconfirmed PMAs have a mean area size of 8,000 m² equivalent to 35 pixels and are often isolated near the mountain ridges or valley floors. From Figure 4 we can state that the ratio confirmed to not-confirmed PMAs increases with PMA size, suggesting that larger objects are more likely to be detected using the L7/8 dataset. Further discussion regarding the possible

14

causes of these polygons can be found in Section 6.2. For the rest of the manuscript, only the 382 confirmed polygons will be considered.

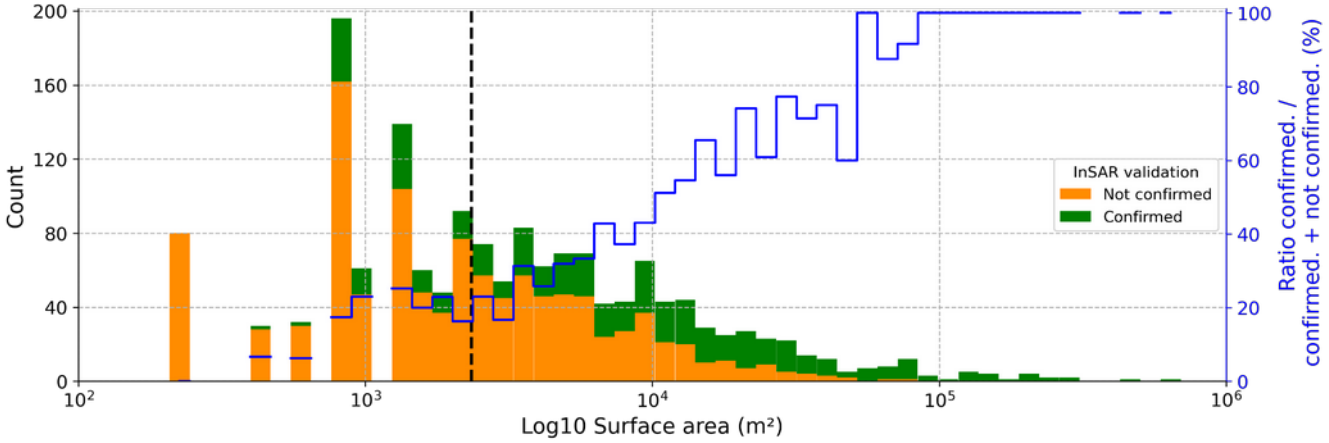

Figure 4: Distribution of raw 'confirmed' and 'not confirmed' PMA by surface area (bins = 50). Black vertical line represents the surface threshold i.e. 2250 m² (10 pixels) used as a filter to remove smaller PMAs. All polygons below the surface threshold were removed. Blue line, represents the ratio between confirmed features over total features by bins. For access to our PMA polygons for our own assessment, refer to the Data availability section.

5.2 Regional distribution of surface velocity

Figure 5a provides an overview of the 24-year average velocity across the central Andes region. For each PMA, a coherent downslope surface velocity field overlaps a sector of a rock glacier (cf. Section 6.3 for discussion). The Top 50% average velocity corresponds to 0.30 m yr-1 over 24 years for all 382 PMAs. The NMAD computed over stable areas corresponds to ±0.07 m yr-1 over the same period (cf. Section 5.4 for a discussion about the uncertainties).

The Top 50% average velocities for each geomorphological class —rock glaciers, landslides, and unclassified— are 0.37 m yr-1, 0.20 m yr-1 and 0.18 m yr-1, respectively. Rock glaciers exhibit a median average velocity 23% higher than the dataset-wide average (Fig. S9). Only three PMAs exceed Top 50% average velocities greater than 2 m yr-1 in Top 50% average velocities, corresponding to the Largo rock glacier (Fig. 2c; Fig. 5c), Olivares and Olivares west complex rock glaciers (Fig. 4f and g) and one landslide. Additionally, eight PMAs have velocities between 1 – 2 m yr-1, including five large rock glaciers and three landslides. The remaining 371 PMAs have average velocities below 1 m yr-1 over 24 years.

In addition to average velocity fields, cumulative displacement time series were obtained for all PMAs (Fig.5; Fig. S9). These time series capture temporal variations such as accelerations or decelerations (Fig. 5e and f). Most of the rock glaciers

15

with mean velocities < 1 m yr-1, show a linear trend in surface displacement (Fig. 5b and d). Annual velocity fluctuations are difficult to assess due to the high uncertainties of individual displacement fields (NMAD between 1.21-3.07 m Table 2).

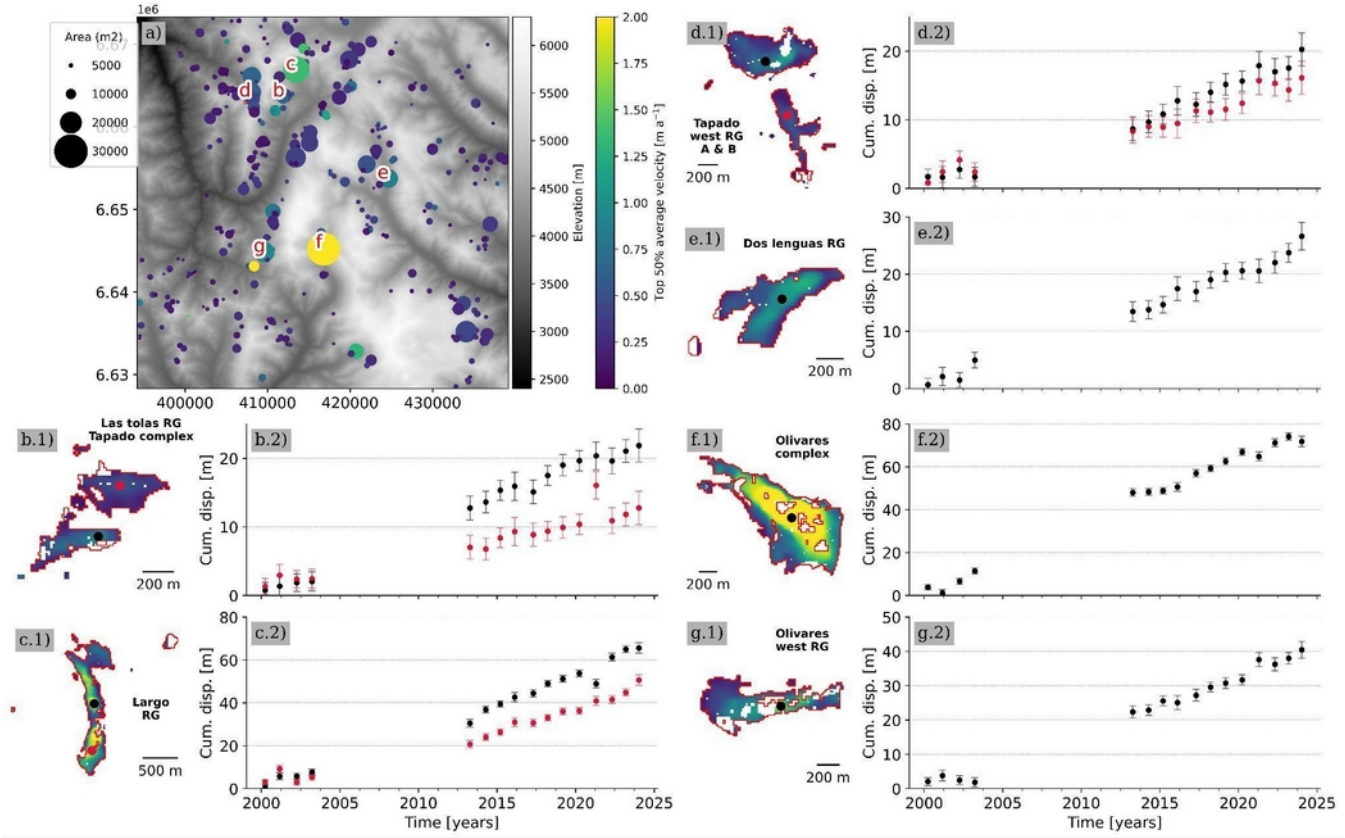

Figure 5: Surface kinematic characterisation for all PMAs in the central Andes region. a) Illustrates the spatial distribution of all valid PMAs (rock glacier = 146; landslide = 115; unclassified = 103) coloured by the 'Top 50% average velocity' surface velocity (viridis colorbar) within the PMA surface. The size of the circle scales with the PMA surface. The red letters correspond to the study cases presented in the following subplots. The remaining subplots b) to g) (with a suffix of *.1) illustrate the mean annual velocity field over the 24 years (2000-2024) for a specific landform (name is displayed in bold), where the magnitude of velocity is coloured using viridis colorbar from panel a). Subplots with a suffix of *.2 represents the cumulative surface displacement time series in metres (subplots with a suffix of *.2), extracted on the black (and red) point within the landform. Error bars show the NMAD on stable areas for each date respectively (Section 5.4). Subplots b) to g) correspond to the following landforms b) Tapado Complex and Las Tolas Rock Glacier; c) Largo Rock Glacier; d) Tapado west Rock Glacier; e) Dos Lenguas Rock Glacier; f) Olivares Complex, g) Olivares west Rock Glacier.

16

5.3 Velocity validation using GNSS and VHR datasets

We compare surface velocity fields for the two selected sub-regions: Tapado complex (Fig. 2c) and Largo rock glacier (Fig. 2d). The first comparison involved GNSS points distributed along the main tongue of Tapado complex and Largo rock glacier—located in the central flow line as well as the borders of the landform—and L7/8 and VHR surface average velocity fields (Figure 6). This point to pixel comparison is shown in Figure 7, where a good agreement between VHR and GNSS and pseudo-GCPs is observed. However, some differences—particularly an underestimation of average velocity—are noticeable at points near the borders of Tapado complex and Largo rock glacier. In addition, some of the fastest points on the Largo rock glacier show important differences.

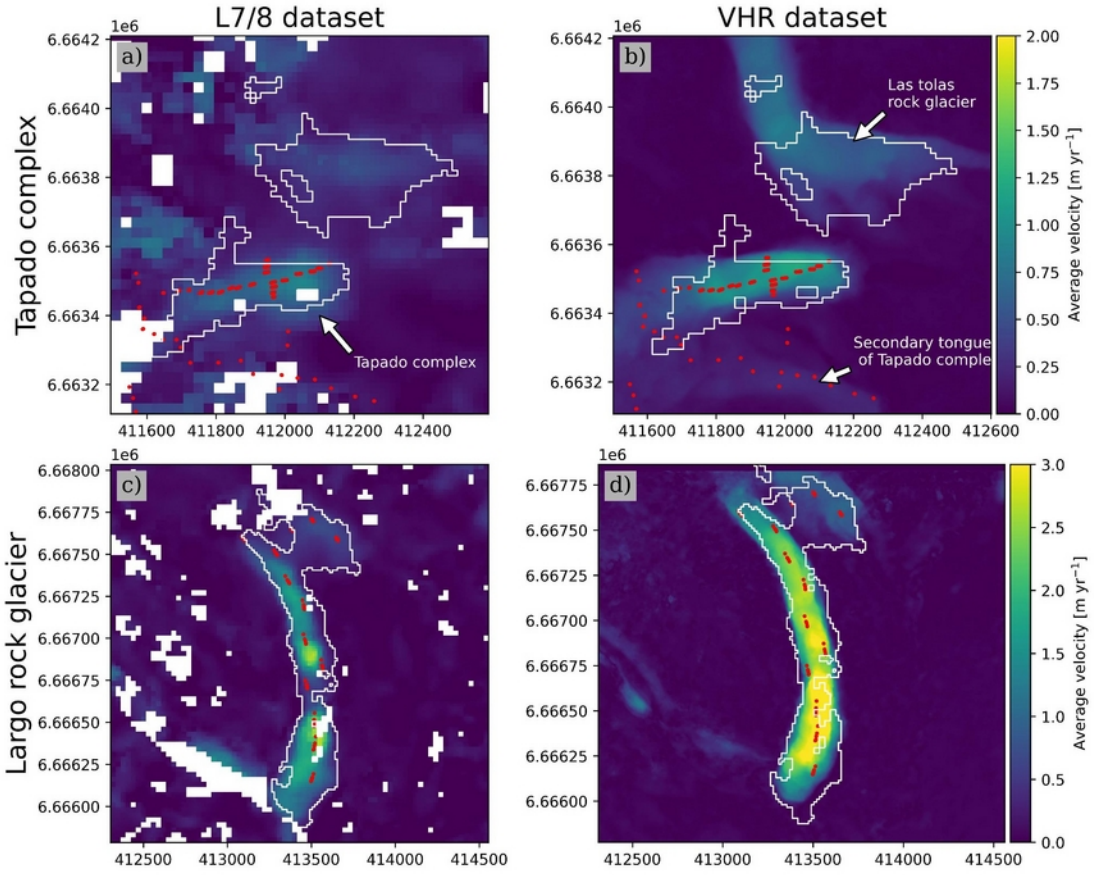

Figure 6: Comparison of mean annual velocity over the 2000-2020 period for Tapado complex a) and b); and Largo rock glacier c) and d) for both L7/8 and VHR dataset, respectively. Red points show the location of GNSS for Tapado complex (CEAZA, 2023) and pseudo-GCP for Largo rock glacier. White polygons correspond to their respective PMAs identified from the L7/8 dataset (cf. Section 3.5).

17

Quantitatively, the average velocity differences between VHR and GNSS points is 0.01 ± 0.05 m yr-1 (Tapado complex) and 0.38 ± 0.3 m yr-1 (Largo rock glacier). Meanwhile, the average difference between L7/8 and GNSS points is 0.18 ± 0.24 m yr-1 (Tapado complex) and 1.35 ± 0.84 m yr-1 (Largo rock glacier; Figure 7). The good agreement on slow surface velocities on the Tapado complex could be explained by the homogeneous surface velocity field in both datasets (Fig. 6a). However, this consistency is not observed on the Largo rock glacier, where large differences are likely due to the heterogeneity of its surface velocity field. Figure 6c shows a single PMA that could be either divided in two, splitting Largo rock glacier in two different units, with likely independent dynamics. This is not the case for the VHR velocity field, showing rather a more homogeneous spatial distribution of velocities (Fig. 6d).

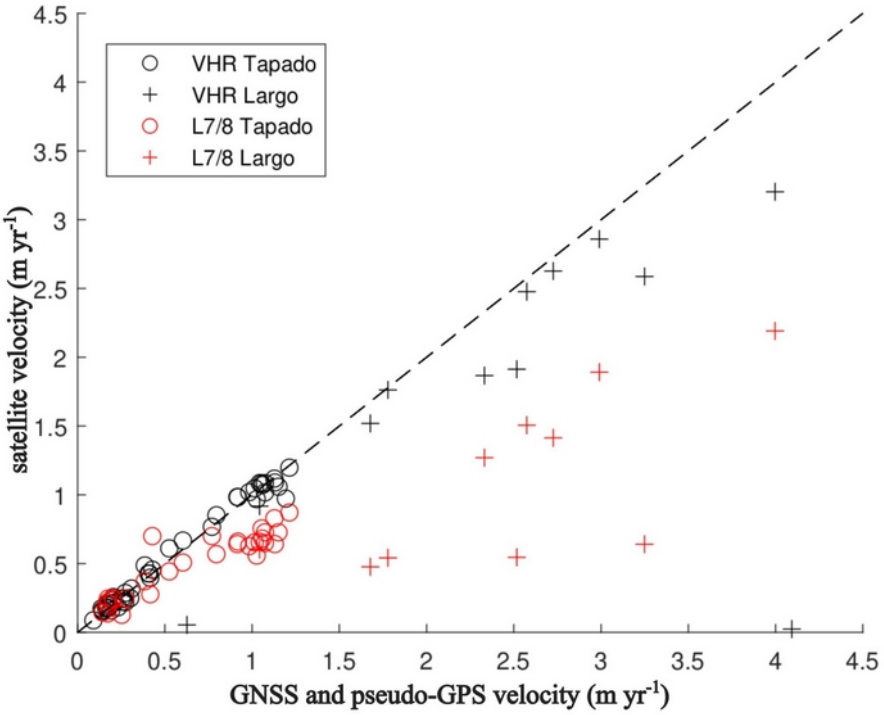

Figure 7: Comparison between GNSS (orpseudo-GCPs) average velocity and average surface velocity fields from both L7/8 (red) and VHR (black) datasets in the subregions of Tapado complex and Largo rock glacier. The average surface velocities from GNSS measurements, L7/8 and VHR datasets, were calculated according to the common time period, spanning from 2009 to 2020.

A detailed comparison with VHR optical imagery revealed a good agreement with GNSS data. The correlation coefficient between two datasets is 0.99 for Tapado complex and 0.45 for Largo rock glacier,respectively, with a linear fit coefficient of 0.99 and 0.44 respectively. The lower correlation at Largo rock glacier is attributed to points situated near the rock glacier

18

borders (Fig. 6, Fig. 7). The correlation between L7/8 and GNSS data is also very good, especially for the Tapado (0.92 and 0.7 for the Tapado and Largo respectively). However, L7/8 tends to always underestimate the velocities (coefficient of the linear fit of 0.69 and 0.45 for the Tapado and Largo rock glaciers; cf. Section 6.1 for further discussion).

5.4 Reported uncertainties

The horizontal accuracy assessment at annual and selected periods in this study is summarized in Table 2. For the L7/8 dataset, the average NMAD of surface displacement over stable areas obtained is 1.8 m in EW and NS components (Table 2)which corresponds roughly to 1/10 of L7/8 pixel size. Individual displacement fields have too high uncertainties to reliably detect significant annual scale velocity changes. However, at decadal timescales, uncertainties decrease significantly (Table 2). The NMAD is 0.21 and 0.19 m yr^{-1}, for 2000-2014 and 2013-2024 periods, respectively. Applying the average NMAD value for both periods as a filter of PMAs, 150 PMAs are above this threshold, being good candidates to depict velocity changes. The 'Top 50% average velocity' at decadal scale of all PMAs is 0.3 m yr^{-1}, 1.5 times larger than the uncertainty.

Table 2. Accuracy and uncertainty assessment of surface displacement and surface velocity at annual and decadal time span. Spatial statistics were computed over a stable area of 53% for L7/8 (n pix = 4 810045), 55 % (n pix = 10 593 874) and 47% (n pix = 3 522 115) for Tapado complex and Largo rock glacier VHR dataset, respectively. [(a)] Values between brackets represent the range (min and max) values over a stable area for each component. [(b)] Difference velocity between GNSS and pseudo-GCPs vs surface velocity fields, computed using the same time period. [(c)] VHR dataset was split in two sub periods trying to fit the same time span as for the L7/8 dataset.

		STABLE AREAS								**MOVING AREAS**	
		Annual surface displacement [m] [(a)]		**Decadal velocity [m yr^{-1}]**				**24-year velocity [m yr^{-1}]**		**Difference in velocity [m yr^{-1}] [(b)]**	
				2000-2014		**2013-2024**		**2000-2024**		**2010-2022**	
L7/8 dataset		**E-W**	**N-S**	**E-W**	**N-S**	**E-W**	**N-S**	**E-W**	**N-S**	**Tapado**	**Largo**
	Mean	[-0.16, 0.45]	[-0.70, 0.20]	-0.009	-0.009	0.032	-0.021	0.004	-0.008	0.183	1.359
	Median	[-0.36, 0.32]	[-0.82, 0.34]	-0.006	-0.014	0.017	-0.023	0.004	-0.015	0.157	1.224
	Std	[2.25, 5.93]	[2.37, 6.03]	0.275	0.298	0.255	0.283	0.136	0.141	0.236	0.837
	Nmad	[1.33, 2.74]	[1.21, 3.07]	0.150	0.148	0.148	0.120	0.093	0.084	0.240	1.001
VHR dataset		**Multi annual surface displacement [m]**		**Decadal velocity [m yr^{-1}] [(c)]**				**20-year velocity [m yr^{-1}]**		**20-year velocity [m yr^{-1}]**	

19

		(a)		2000-2014		2012-2020		2000-2020		2010-2022	
		E-W	**N-S**	**E-W**	**N-S**	**E-W**	**N-S**	**E-W**	**N-S**	**Tapado**	**Largo**
	Mean	[-0.05, 0.11]	[0.19, 0.06]	0.010	-0.012	-0.002	-0.006	0.005	0.002	0.011	0.377
	Median	[-0.23, 0.0]	[-0.23, 0.06]	-0.011	-0.020	-0.002	0.000	-0.012	-0.012	0.006	0.206
	Std	[0.35, 1.34]	[0.31, 1.16]	0.120	0.097	0.049	0.054	0.078	0.065	0.047	0.307
	Nmad	[0.11, 0.36]	[0.28, 1.00]	0.030	0.078	0.030	0.010	0.020	0.048	0.036	0.133

5.5 Velocity changes

Using the 24-year surface displacement dataset, decadal velocity changes (Eq. 1) and velocity change uncertainties (Eq. 2) were computed using Top 50% average velocity over two periods: 2000–2014 (V_1) and 2013–2024 (V_2), across all PMAs. However, since relative velocity changes depend on the initial velocity magnitude (Eq. 1), velocity changes on PMAs with smaller magnitudes (<0.3 m yr^{-1}) exhibit higher uncertainties. According to our calculations, only 2% (n = 8) of the entire PMA dataset exhibits velocity changes greater than their respective uncertainties (σV_{change};Fig. 8). Among these, 3 rock glaciers, 2 landslides, and 3 unclassified PMAs, were identified. These 3 rock glacier PMAs have an average size of 6,075 m² (~27 pixels) with a Top 50% average velocity of 0.59 m yr^{-1}. Two (one) of them, accelerate (decelerate) with a mean value of 198% (-46%). Landslide PMAs have an average size of 15,412 m² (~69 pixels) and a Top 50% average velocity of 2.5 m yr^{-1}. However, only 2 cases exhibit acceleration with a mean of 214%. PMAs in the 'unclassified' class have an average size of 7,050 m² (~31 pixels) and a Top 50% average velocity of 0.44 m yr^{-1}. One (two) accelerates (decelerates) with a mean value of 70% (-42%).

20

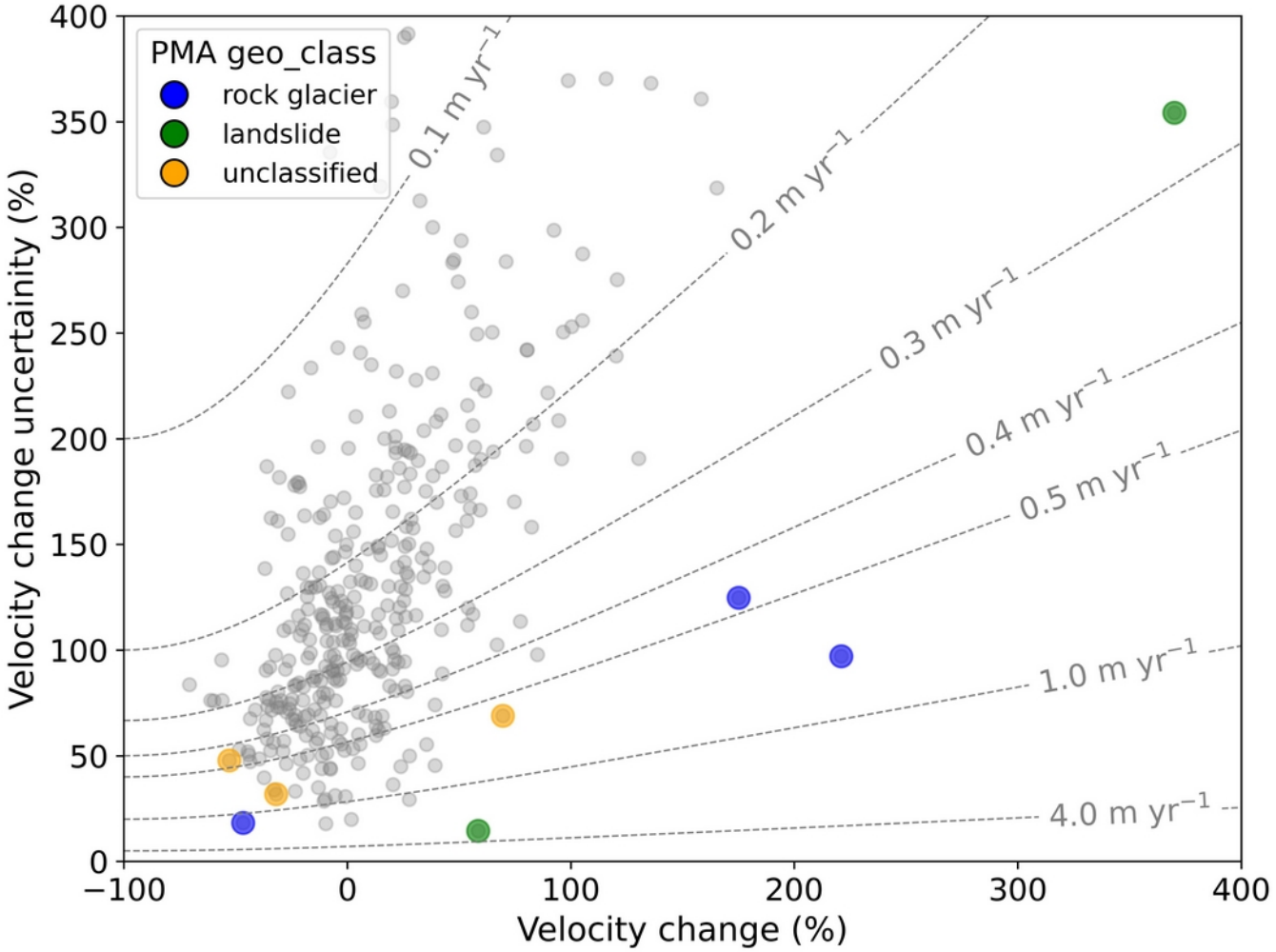

433 **Figure 8.** Modeling of relative velocity changes (dashed lines; Eq. 1) and their respective uncertainties (Eq. 2) for various
434 velocity magnitudes (0.1 – 4 m yr^{-1}). Grey dots represent the entire PMA dataset. Blue, green and orange dots highlight
435 PMAs where velocity changes exceed their uncertainties.

436 **6 Discussion**

437 Rock glacier velocities are typically estimated using high resolution optical data (e.g. Pellet et al., 2022) and SAR remote
438 sensing imagery (Strozzi et al., 2020, Villarroel et al., 2018), but these datasets are prohibitively expensive for larger areas
439 and/or relatively recent, covering only the past 20 years (Toth & Jóźków, 2016). In contrast, Landsat imagery (e.g. L4-5-7 or
440 L8) extends back to the mid-1980s (Kooistra et al., 2024; Ustin and Middleton, 2021). In this context, freely accessible L7/8
441 imagery emerges as a valuable source for studying rock glacier kinematics over extensive spatial and temporal scales
442 (Lacroix et al., 2020b). To the best of our knowledge, this is the first time that Landsat imagery is being employed to monitor

21

rock glacier displacement time-series and derive velocity changes. This analysis is enabled by combining robust methods, including information redundancy, time-series inversion and the persistent moving area detection, which make L7/8 data viable for rock glacier monitoring. Nonetheless, certain limitations and future perspectives regarding the use of Landsat imagery for rock glacier kinematics analysis must be addressed.

6.1 Intrinsic limitations on the remote sensing datasets

The primary technical consideration is the spatial resolution of the L7/8 dataset (15 m in the panchromatic band). This pixel size is coarse relative to the region's average surface velocity (i.e. ~1 m yr^{-1}; Vivero et al., 2021; Halla et al., 2021). This method is therefore best suited for fast-moving rock glaciers. In regions with large rock glaciers, such as the Andes or the High Mountain of Asia (Sun et al., 2024), medium-resolution L7/8 imagery can provide new insights into the temporal dynamics of rock glaciers. Here, a minimum surface threshold of 2250 m^2 (10 pixels) proves effective for the Andes but may be less suitable for regions with smaller rock glaciers, such as the European Alps, where features may fall below the detection threshold. The 15 m spatial resolution also limits the ability to capture fine details, thus small-scale spatial variations in velocity. Figure 6 illustrates how pixel size affects boundary delineation: in the Tapado complex, the secondary tongue (Fig. 6a, b)—moving at 0.25–0.5 m yr^{-1} (Vivero et al., 2021)—appears indistinct, with gaps and noise in displacement fields (Fig. 6a), as does the adjacent Las Tolas rock glacier. Despite this, the automatic PMA extraction (Section 3.4) successfully identifies a coherent PMA across much of Las Tolas' tongue (Fig. 6a), demonstrating this filter's potential for detecting active rock glaciers, even in high altitude regions where snow and shadows introduce noise in image correlation (Cusicanqui et al., 2023).

Another key consideration is the surface roughness and texture of rock glaciers, for instance features like ridges and furrows, which appear less detailed in L7/8 than in the VHR dataset (Fig. 2c). This can impact the feature tracking performance (Heid and Kääb, 2012). For example, on the main tongue of the Tapado complex (Fig. 6a), L7/8-derived surface velocity is consistent with GNSS data (0.01 ± 0.05 m yr^{-1}). While the 24-year average surface velocities align with Vivero et al., (2021), a discrepancy of 0.1–0.2 m yr^{-1} is observed, likely due to L7/8's image resolution. Similar differences occur on the Dos Lenguas rock glacier, which has an average velocity of 1.5–2 m yr^{-1} (Halla et al., 2020; Strozzi et al., 2020), while L7/8 imagery shows average velocities of 1.1–1.5 m yr^{-1} (Fig. 5e). In contrast, Largo rock glacier presents greater complexity. Despite its ridge-and-furrow morphology, its homogeneous texture (Fig. 2d) reduces contrast, potentially explaining observed discrepancies between the L7/8 and VHR results (3–4 m yr^{-1}; Figure 6b). Velocity estimates in landforms with high spatial heterogeneity are highly affected by the L7/8 resolution, which captures less surface details. Therefore, correlation parameters are key when performing image correlation (Heid and Kääb, 2012; Leprince et al., 2008; Rosu et al., 2015). As L7/8's smallest matching window (3x3 pixels, covering 2025 m^2) differs substantially from the VHR window (7x7 pixels, covering 49 m^2) leading to an averaging effect. This difference contributes to the observed variability in features such as

22

Largo rock glacier. Finally, solar illumination changes introduce shadow-induced noise in image correlation (Dehecq et al., 2015), which was minimized by selecting L7/8 images mainly from March (with a few from January).

6.2 Validation of PMA using InSAR and local rock glacier inventories

The average velocity fields from L7/8 optical satellite data align well with Sentinel-1 interferograms and their interpretation (Fig. S16) when comparing InSAR wrapped interferograms and PMA characterisation. However, this comparison is affected by different uncertainties: (i) while S1 interferograms show only LOS motion, limiting the discrimination of lateral and vertical movements (Barboux et al., 2014), optical imagery provides both horizontal components of surface kinematics; (ii) . Not confirmed PMAs, often located in low-relief areas, near riverbeds, or close to ridges (Fig. S2), are likely due to the smoothed DEM used as slope direction reference or shadows in L7/8 images. Some PMAs also appear near human settlements, including mining sites, where InSAR did not indicate displacement;(iii) Interferograms reflect movements over short time intervals (e.g. 12 days,or 60 days, etc) within a limited time-period (2022-2023), potentially missing gravitational movements that were inactive at that time; (iv) InSAR velocity classes for PMAs followed RGIK (2023) recommendations, though FLATSIM interferograms have a coarser pixel size (30 m) than those in Strozzi et al., (2020) or Bertone et al., (2021), making fringe patterns difficult to discern, specially for small landforms.

Some PMAs cover complex landforms with diffuse boundaries, and thus were assigned requiring a general geomorphological classification without specific discriminations, including debris-covered glaciers and glacier-rock glacier transitions (Monnier & Kinnard, 2015, 2016). Additionally, PMAs categorized as ‘unclassified’ lack clear geomorphological features for a complete interpretation. Rock glaciers are slightly better detected than landslides, likely due to the lower motion variability with time. Rock glaciers are viscous flows (Haeberli et al., 2006) undergoing activity changes over long periods (Kellerer-Pirklbauer et al., 2022; Lehmann et al., 2021; 2025). In contrast, landslides are influenced by seasonal and transient patterns (Lacroix et al., 2020b).

A comparison with existing rock glacier inventories for the Chilean (DGA, 2022) and Argentinian (IANIGLA, 2018) Andes was conducted, focusing on PMAs classified as rock glaciers only (n = 153). Using Ch-Arg rock glacier inventory as a reference, 68% of the PMAs (n = 104) intersects the existing inventory at an average of 30% of their surface area (Fig. S12). However, only 20% of the overlapping PMAs (n = 20) coincide with more than 50% of their surface. The remaining 32% of the PMA (n = 49) are unmapped rock glaciers identified through L7/8 optical imagery and validated with InSAR (RGIK, 2023). This comparison relies on the accuracy of the Ch-Arg rock glacier inventories, which contains certain ambiguities. For instance, the Chilean inventory, released in 2013 and updated in 2022 (DGA, 2022), overrepresented rock glaciers by including headwall sections (Fig. S12), while the Argentinian inventory defines rock glacier boundaries more conservatively. Neither of the two inventories has yet been updated according to RGIK guidelines (RGIK, 2023). Finally, InSAR velocity

23

data indicate that 69% of the rock glacier PMAs (n = 105) were detected using 12-day interferograms (Fig. S16), suggesting a velocity class between 30–100 cm yr^{-1} (RGIK, 2023), consistent with our results.

6.3 Average PMA surface velocity

Since our dataset provides a spatial representation of surface displacement for 382 PMAs—comprising 153 rock glaciers, 124 landslides and 105 non-classified landforms—we pose the following question: what is the most appropriate threshold for computing average surface velocity fields? Computing statistics per landform using the same threshold is challenging due to the large pixel size of L7/8 imagery and the varying PMA sizes. When spatial average velocities are computed using the Top 50% pixels, bias resulting from lateral variability is minimized, and only the central portion of the PMA is conserved, corresponding to the fastest area (see Fig. S15 for a comparison). This methodology inspired from Blöthe et al., (2021) ensures that the fastest area is selected independently for each PMA based solely on 24-year average velocity. However, using different thresholds can lead to overestimations of average velocity. Figure 9 quantifies the impact of selecting 'Top 50%, 30% and 10% average velocity. The mean difference between the full-PMA average velocity and the 'Top 50%, 30% and 10% velocities' corresponds to 20%, 31% and 44%, respectively. These differences underscore the significance of selecting an appropriate threshold. Here, we consider that the 'Top 50% average velocity' computed over a 24-year period represents an optimal compromise preserving average velocity field while minimizing lateral effects and maintaining a sufficient number of pixels within the PMA. This approach also reduces the operator-induced ambiguity. Nevertheless, further studies should be conducted to evaluate this metric using different temporal intervals and with different remote sensing datasets.

24

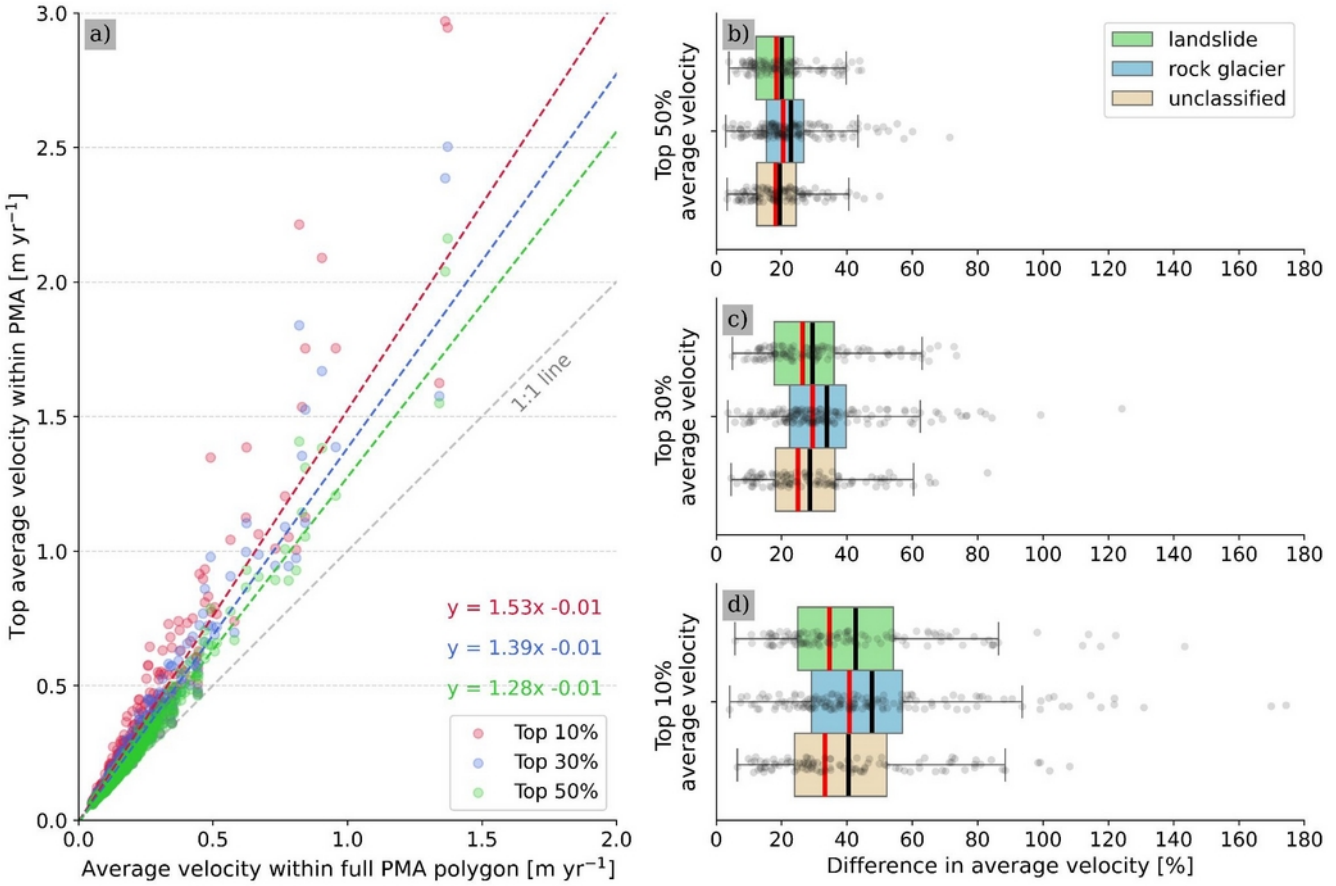

526 **Figure 9:** a) Comparison between average velocity computed using the entire PMA surface and 'Top 50%, 30% and 10%
527 average velocity' within PMA. Subplots b), c), and d) show the difference of average velocity 'Top 50%, 30% and 10%
528 average velocity' with respect to the average velocity computed over the entire PMA surface.

529 **6.4 Surface velocity variations and uncertainties**

530 Regarding uncertainties in those PMA with GNSS data—Tapado and Largo rock glaciers—our approach generally
531 underestimates surface velocities by 10–20% on average (Fig. 7). Tapado velocities (1–2 m yr^{-1}) align well with GNSS data,
532 whereas Largo velocities (2–4 m yr^{-1}) are underestimated by 30–40%, likely due to textural differences and lack of contrast
533 on L7/8 dataset (Section 6.1). The overall underestimation of surface velocities in L7/8 imagery could be attributed to the
534 large pixel size (15 m), which reduces pixel counts per matching window. Calculations show an NMAD of surface velocities
535 over 24-year on stable areas of 0.07 m yr^{-1} ± 0.16 (1σ), similar to uncertainties found by Kääb et al., (2021) in the Tien Shan
536 region using high-resolution historical images with poor scan quality and by Wood et al., (2025), using a single pair of
537 Landsat imagery in the same region. In contrast, Blöthe et al., (2021), using a Limits of Detection (LoD) method with high-

resolution optical images, reported uncertainties from 0.28 to 0.5 m yr^{-1}. The low uncertainties reported from L7/8 imagery over a 24 years support the reliability of our interpretation.

However, annual velocity uncertainties are notably higher than those estimated over the entire period (Table 2). The NMAD of consecutive displacements over stable areas (Fig. S3) is 1.8 m ± 0.33, consistent with previous studies (Lacroix et al., 2019; Scherler et al., 2008), using L7/8 images. Only 2% of PMAs (n = 8) were retained by applying this NMAD as LoD filter (Blöthe et al., 2021), corresponding to large and fast rock glaciers (Fig. 5c, f, and g). This analysis demonstrates that L7/8 imagery allows kinematic characterization of rock glaciers over large periods of time (10-20 years) but not for annual velocity variations.

Regarding decadal velocity changes uncertainties between 2000-2014 and 2013-2024 , three main factors contribute:

- **Observation discrepancies:** The 2000-2014 period includes only six images due to a gap between 2003 and 2013, whereas 2013 to 2024 has 11 years of continuous observations. This imbalance may bias average velocity and conditioning related uncertainties (Fig. 5; Fig. 8). Using ASTER or other medium-resolution imagery could help to fill this gap, despite its low radiometric resolution (Lacroix et al., 2022).
- **PMA size:** L7/8 imagery performs better on larger landforms with more pixels. Velocity change uncertainties are higher at PMA borders due to the lower velocity magnitudes and the lateral discontinuity, less pronounced on bigger PMAs. However, larger PMAs obtained in this study are linked to complex processes (e.g. glacier-permafrost interactions) which may have influenced internal landform variability. The Largo rock glacier exhibits a velocity increase of +54% and +29% in L7/8 and VHR datasets, respectively. Conversely, the Olivares ice-debris complex (debris-covered glacier connected), showed a -9% velocity change in one decade using L7/8 data. Similar patterns were observed 100 km south of Elqui valley (Monnier et al., 2014; Monnier and Kinnard, 2013, 2015), as well as in the Tien Shan region (Kääb et al., 2021), the European Alps (Cusicanqui et al., 2023; Gärtner-Roer et al., 2021; Kunz and Kneisel, 2020). These observations suggest that complex interactions between glacier retreat and permafrost-related landforms influence surface velocities, highlighting the need for further research.
- **Andean velocity observations:** Limited Andean studies report significant velocity changes in recent decades. Vivero et al., (2021) found a 7% of acceleration in the 2000-2020 decades. Our VHR data show limited changes, with -3 ± 10 % slow-down in the Tapado complex and +14 ± 10 % speed-up in Largo rock glacier between 2000-2010 and 2010-2020. Over 40 years, Vivero et al. (2021) observed a 0.2 m yr^{-1} acceleration in Tapado complex, representing a 25% increase in velocity. Such a level of acceleration might not be detected by L7/8 imagery due to the too low velocity. Further studies could benefit from incorporating older datasets, like SPOT 1-4 up to the mid 1980's or Corona images from the 1960s (Dehecq et al., 2020; Kääb et al. 2021).

6.5 Wider geomorphic implications of PMAs

Understanding the broader geomorphic implications of PMAs is critical for interpreting their role in high mountain environments and their response to climatic and geomorphological processes. While this study primarily focuses on kinematic and spatial characteristics of PMAs, this section contextualizes the observed patterns within a regional framework. By bridging findings with topographic and geomorphological contexts, we highlight the factors influencing PMA spatial distribution and surface dynamics. The PMAs in the study area show heterogeneous spatial distribution across topographic conditions (Fig. 5a). Analysis of the Top 50% average velocity in relation to slope, aspect, elevation and surface area—derived from the TanDEM-X 12.5 m DEM—reveals several key patterns (Fig. 10, Fig. S7)

- Rock glaciers predominantly occur uniformly on slopes of 10–35°, while 'landslides' and 'unclassified' features are concentrated on steeper slopes (>25°), peaking at 30° and 35°, respectively. This pattern aligns with the regional slope distribution, suggesting slope as a key control for landslides and unclassified landforms (Fig. 10a).
- Slope aspect varies distinctly by landform type. Rock glaciers primarily face West to South and East, consistent with regional permafrost models (Gruber, 2012, Obu, 2021; Azocar et al., 2017). In contrast, 'landslides' and 'unclassified' features predominantly occur on northwest to east-facing slopes (Fig. 10d). Similar findings from Blöthe et al., (2021) in the Cordon del Plata underscore slope orientation as a key controlling factor.
- Most rock glaciers with velocities between 1–2 m yr^{-1} are located at 4,500–5,000 m a.s.l., although no strong correlation with altitude was found. Conversely, 'landslide' and 'unclassified' PMAs occur at lower elevations (~3500 m a.s.l.), often where permafrost is heterogeneous or discontinuous (Gruber 2012; Azócar et al., 2017) (Fig. 10b).
- In the Top 50% average velocity category, larger rock glaciers exhibit higher surface velocities, unlike 'landslide' and 'unclassified' PMAs (Fig. 10c). This may reflect specific and local geomorphological conditions, such as the accumulation zone at Largo rock glacier, where material influx likely drives (Janke and Frauenfelder, 2008) surface acceleration (+54% in the L7/8 dataset) (Janke and Frauenfelder, 2008). By contrast, Olivares ice-debris complex shows deceleration, potentially linked to ice-mass loss in adjacent debris-covered glaciers. Similar patterns have been observed in the Tien Shan region (Kääb et al., 2021) and more recently in the European Alps (Manchado et al., 2024). Further studies are necessary to understand the mechanics of these complex landforms.

Although this study focuses on monitoring rock glaciers on a regional scale, it also identifies other PMAs corresponding to landslides and some unclassified landforms. Our results suggest possible correlations between gravitational movements in high mountain areas (e.g. Haeberli et al., 2017; Patton et al., 2019) and permafrost degradation (i.e. freeze, thaw of permafrost) in recently deglaciated areas (Pánek et al., 2022). This study contributes to existing mass movement inventories

27

in the region (e.g. Iribarren Anacona et al., 2015), highlighting areas for further research. While these findings provide valuable regional insights into surface kinematics and topographic relationships, they must be interpreted cautiously. The morphological statistics here are derived solely from PMA boundaries and may not fully represent entire landforms (Fig. S12). Additionally, PMAs exclude feeder basins, responsible for material and water supply to the rock glacier (Blöthe et al., 2021; Cusicanqui et al., 2021). Further studies should be conducted to look at the influences of feeder basins on surface kinematics of rock glaciers.

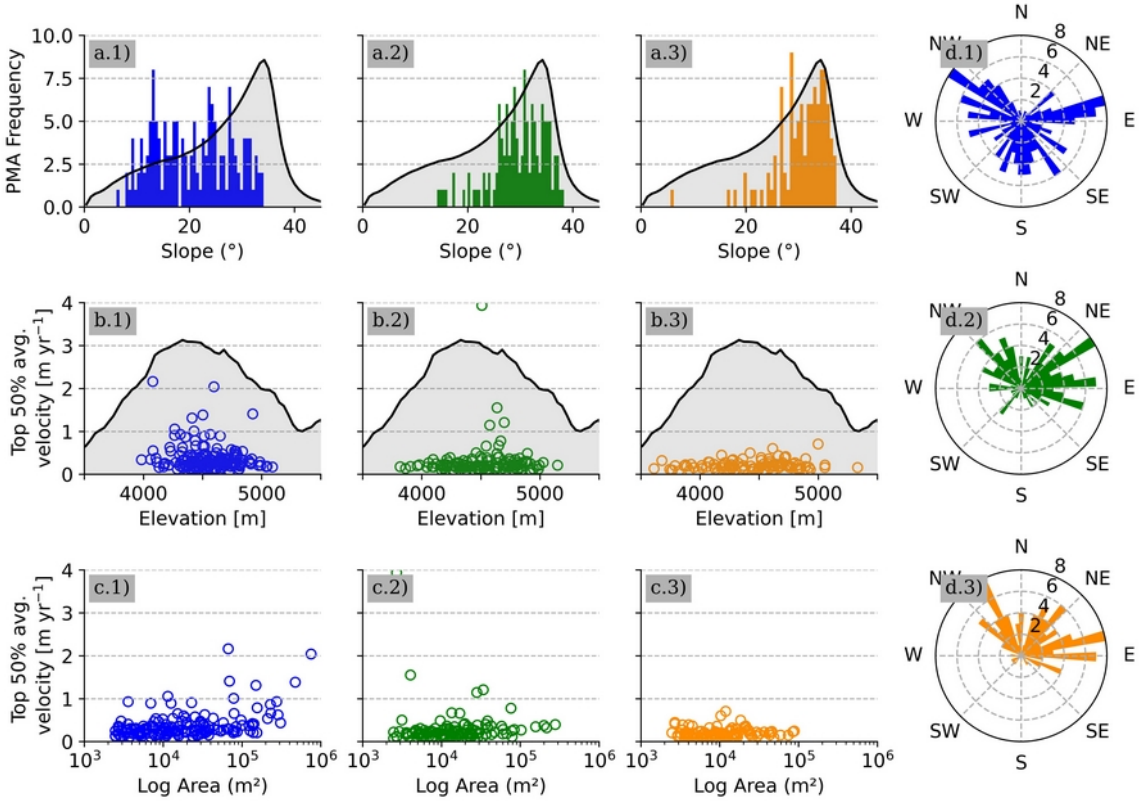

Figure 10: Comparison of the PMA distribution for 'rock glacier' (blue values), 'landslide' (green values) and 'unclassified' (orange values) geomorphological class vs regional topographical context (computed using average pixel frequency from TanDEM-X 12 m DEM). a) PMA mean slope; b) distribution between Top 50% average velocity PMA and PMA mean elevation; c) distribution between Top 50% average velocity and PMA surface; d) PMA slope orientation. For a) and b), the grey background represents the general slope and elevation distributions of the study area, respectively.

6 Conclusions

This study develops a robust method to detect, quantify, and analyse the surface kinematics of rock glaciers and other gravitational mass movements using time series of Landsat 7/8 imagery. By integrating feature tracking over 24 years with

28

time-series inversion and automatic detection of persistent moving areas (PMA), we successfully monitor 153 rock glaciers, 124 landslides and 105 unclassified landforms over a 45x45 km² area in the semiarid Andes. The validation with satellite radar interferometry confirms the PMA classification and their velocity attributes, with 42% also detected by Sentinel-1 interferograms at 12-day temporal baselines. Faster-moving landforms (2–4 m a^{-1}), primary complex ice-debris landforms, were detected. The 24-year average velocity of PMAs is 0.3 ± 0.07 m yr^{-1}, with rock glaciers moving 23% faster than the median velocity of all geomorphological landforms. Faster-moving landforms (2–4 m yr^{-1}), primary complex ice-debris landforms, were detected. Although some underestimations occur due to the coarse pixel size, temporal data gaps and velocity field heterogeneity, decadal velocity changes were detectable for 2% of PMA dataset (n = 8). Among these PMAs, we find acceleration (deceleration) in 2 (1) rock glaciers, 2 landslides, and 1 (2) unclassified PMAs, all exceeding their respective uncertainties. According to our calculations, detecting decadal velocity changes below 0.4 m yr^{-1} (two times decadal NMAD values) using L7/8 data involves high uncertainty, depending on both velocity magnitude and the length of the reference period. The results of this study aligned well with existing research, highlighting the potential of combining radar and optical remote sensing to improve the detection and monitoring of slow and fast gravitational mass movements. These findings enhance rock glacier mapping and kinematic understanding, particularly in the context of permafrost warming and its impact on periglacial landforms. This study demonstrates the capability of medium-resolution L7/8 imagery for quantifying the kinematics of rock glaciers and ice-debris complex dynamics at a regional scale. It provides a methodological benchmark for assessing dynamics of periglacial landforms using globally accessible, open-source optical imagery, addressing a key need within the scientific community.

Code availability. Feature tracking image correlation softwares used for this study are open-source softwares. Ames Stereo Pipeline (ASP) is available from https://stereopipeline.readthedocs.io/en/latest/introduction.html (Beyer et al., 2018) and MicMac is available from https://micmac.ensg.eu/index.php/Accueil (Rupnick et al., 2017). Time-series inversion from optical imagery (TIO) is available from https://sourcesup.renater.fr/www/tio/. Sentinel-1 interferograms were computed using ForM@Ter LArge-scale multi-Temporal Sentinel-1 InterferoMetry processing chain (FLATSIM) based on the NSBAS pipeline. Both are available through GDM-SAR service at https://www.poleterresolide.fr/le-service-gdm-sar-in/.

Data availability. Landsat 7/8 archive freely available at http://earthexplorer.usgs.gov/. Sentinel-1 data used in our study are freely available from the ESA/EC Copernicus Sentinels Scientific Data Hub at https://scihub.copernicus.eu (Copernicus Open Access Hub, 2021). FLATSIM Sentinel-1 interferograms can be accessible upon request via Form@Ter pole (https://www.poleterresolide.fr/). TanDEM-X data are available from DLR through proposal application procedures. Data from Digital-Globe satellites (GeoEye, Ikonos, WorldView, Quickbird) and Pléiades are commercial, but programmes to facilitate academic access exist. Pleiades dataset can be accessed upon request to Ben Robson (Benjamin.Robson@uib.no). The data described in this manuscript are available at (https://zenodo.org/uploads/13119042; Cusicanqui et al., 2024) or upon request from the corresponding author (diego.cusicanqui@univ-grenoble-alpes.fr).

649

650 *Supplement.* The supplement related to this article is available online at: https://zenodo.org/uploads/13119042.

651

652 *Author contributions.* DC, PL and XB designed the study. DC performed image correlation of VHR data provided by BR
653 and XB. PL performed image correlation of L7/8 data and implemented persistent moving area (PMA) detection. DC and PL
654 filter GNSS dataset provided by SM and compute GNSS surface velocity time-series. DC wrote the paper with the
655 supervision and contributions of PL. PL, XB, BR, AK and SM contributed to the discussion and edited the paper.

656

657 *Competing interests.* The authors declare that they have no conflict of interest.

658

659 *Acknowledgment.* Thanks are due to reviewers for their careful review and comments. We are grateful to the providers of
660 free data for this study: European Space Agency (ESA)/European Commission (EC) Copernicus for Sentinel-1 data, the
661 FLATSIM Form@TER team for their efforts processing Sentinel interferograms. Also, the German Aerospace Center (DLR)
662 provides the TanDEM-X DEM. We are grateful to CNES/Airbus DS for the provision of the SPOT and Pléiades satellite to
663 the restrained dataset project 41743. We would like to thank the U.S. Geological Survey for making the Landsat 7/8 archive
664 freely available. Thanks to GLIMS database http://glims.org/RGI/ for glacier outlines (v.6). All (or most of) the
665 computations presented in this paper were performed using the GRICAD infrastructure (https://gricad.univ-grenoble-
666 alpes.fr), which is supported by Grenoble research communities. Thanks to the glaciology group at CEAZA for collecting
667 and providing the GNSS datasets, and the CHESS-funded (https://chess.w.uib.no/) "Summer school on cryospheric
668 monitoring and water resources" for the 2022 acquisition set.

669

670 *Financial support.* This work has been supported by the postdoctoral program from the National Centre for Space Studies
671 (CNES) and partially by the National Center for Scientific Research (CNRS), the program Plan d'Action pour la Prévention
672 des Risques d'Origine Glaciaire et périglaciaire (PAPROG). This work has also been partially supported by a grant from
673 Labex OSUG (Investissements d'avenir – ANR10 LABX56) PermANDES project. Data provided by CEAZA was supported
674 by ANID-CENTROS REGIONALES R20F0008. Diego Cusicanqui (CNES | ISTerre), Pascal Lacroix (IRD | ISTerre),
675 Xavier Bodin (EDYTEM | CNRS) are part of Labex OSUG (ANR10 LABX56). AK acknowledges financial support by the
676 European Space Agency projects Permafrost_cci and EarthExplorer10 Harmony (4000123681/18/I-NB,
677 4000135083/21/NL/FF/ab).

678 **References**

679 Arenson, L., Colgan, W., and Marshall, H. P.: Chapter 2 - Physical, Thermal, and Mechanical Properties of Snow, Ice, and
680 Permafrost, in: Snow and Ice-Related Hazards, Risks and Disasters, edited by: Shroder, J. F., Haeberli, W., and Whiteman,
681 C., Academic Press, Boston, 35–75, https://doi.org/10.1016/B978-0-12-394849-6.00002-0, 2015.

682 Ayoub, F., Leprince, S., Binet, R., Lewis, K. W., Aharonson, O., and Avouac, J. P.: Influence of camera distortions on
683 satellite image registration and change detection applications: 2008 IEEE International Geoscience and Remote Sensing
684 Symposium - Proceedings, 2008 IEEE International Geoscience and Remote Sensing Symposium - Proceedings, II1072–
685 II1075, https://doi.org/10.1109/IGARSS.2008.4779184, 2008.

686 Azócar, G. F. and Brenning, A.: Hydrological and geomorphological significance of rock glaciers in the dry Andes, Chile
687 (27°-33°S): Rock Glaciers in the Dry Andes, Permafrost Periglac. Process., 21, 42–53, https://doi.org/10.1002/ppp.669,
688 2010.

689 Azócar, G. F., Brenning, A., and Bodin, X.: Permafrost distribution modelling in the semi-arid Chilean Andes, The
690 Cryosphere, 11, 877–890, https://doi.org/10.5194/tc-11-877-2017, 2017.

691 Barboux, C.: Detection, mapping and monitoring of slope movements in the Alpine environment using DInSAR., PhD,
692 University of Fribourg, 212 pp., 2014.

693 Berthling, I.: Beyond confusion: Rock glaciers as cryo-conditioned landforms, Geomorphology, 131, 98–106,
694 https://doi.org/10.1016/j.geomorph.2011.05.002, 2011.

695 Bertone, A., Barboux, C., Bodin, X., Bolch, T., Brardinoni, F., Caduff, R., Christiansen, H. H., Darrow, M. M., Delaloye, R.,
696 Etzelmüller, B., Humlum, O., Lambiel, C., Lilleøren, K. S., Mair, V., Pellegrinon, G., Rouyet, L., Ruiz, L., and Strozzi, T.:
697 Incorporating InSAR kinematics into rock glacier inventories: insights from 11 regions worldwide, The Cryosphere, 16,
698 2769–2792, https://doi.org/10.5194/tc-16-2769-2022, 2022.

699 Beyer, R. A., Alexandrov, O., and McMichael, S.: The ames stereo pipeline: NASA's open source software for deriving and
700 processing terrain data, Earth and Space Science, 5, 537–548, https://doi-org.insu.bib.cnrs.fr/10.1029/2018EA000409, 2018.

701 Blöthe, J. H., Halla, C., Schwalbe, E., Bottegal, E., Trombotto Liaudat, D., and Schrott, L.: Surface velocity fields of active
702 rock glaciers and ice-debris complexes in the Central Andes of Argentina, Earth Surface Processes and Landforms, 46, 504–
703 522, https://doi.org/10.1002/esp.5042, 2021.

704 Bolch, T., Shea, J. M., Liu, S., Azam, F. M., Gao, Y., Gruber, S., Immerzeel, W., Kulkarni, A., Li, H., Tahir, A., Zhang, G.,
705 Zhang, Y., Bannerjee, A., Berthier, E., Brun, F., Kääb, A., Kraaijenbrink, P., Moholdt, G., Nicholson, L., Pepin, N., and
706 Racoviteanu, A.: Status and change of the cryosphere in the Extended Hindu Kush Himalaya Region, in: The Hindu Kush

Himalaya Assessment, edited by: Wester, P., Mishra, A., Mukherji, A., and Shrestha, A. B., Springer, 209–255, https://doi.org/10.1007/978-3-319-92288-1_7, 2019.

Bontemps, N., Lacroix, P., and Doin, M.-P.: Inversion of deformation fields time-series from optical images, and application to the long term kinematics of slow-moving landslides in Peru, Remote Sensing of Environment, 210, 144–158, https://doi.org/10.1016/j.rse.2018.02.023, 2018.

CEAZA: Reporte anual 2012. Avalaible at www.ceazamet.cl. Accessed on Febraury 15, 2024, 2012.

CEAZA: Reporte anual 2016. Avalaible at www.ceazamet.cl. Accessed on Febraury 15, 2024, 2016.

CEAZA: Datos meteorologicos proveidos por el CEAZA. obtenidos desde. www.ceazamet.cl. Avalaible at www.ceazamet.cl. Accessed on Febraury 15, 2024, 2023.

Cicoira, A., Beutel, J., Faillettaz, J., and Vieli, A.: Water controls the seasonal rhythm of rock glacier flow, Earth and Planetary Science Letters, 528, 115844, https://doi.org/10.1016/j.epsl.2019.115844, 2019.

Cusicanqui, D., Rabatel, A., Vincent, C., Bodin, X., Thibert, E., and Francou, B.: Interpretation of Volume and Flux Changes of the Laurichard Rock Glacier Between 1952 and 2019, French Alps, Journal of Geophysical Research: Earth Surface, 126, e2021JF006161, https://doi.org/10.1029/2021JF006161, 2021.

Cusicanqui, D., Bodin, X., Duvillard, P.-A., Schoeneich, P., Revil, A., Assier, A., Berthet, J., Peyron, M., Roudnitska, S., and Rabatel, A.: Glacier, permafrost and thermokarst interactions in Alpine terrain. Insights from seven decades of reconstructed dynamics of the Chauvet glacial and periglacial system (Southern French Alps), Earth Surface Processes and Landforms, 48, 2595–2612, https://doi.org/10.1002/esp.5650, 2023.

Dehecq, A., Gourmelen, N., and Trouve, E.: Deriving large-scale glacier velocities from a complete satellite archive: Application to the Pamir–Karakoram–Himalaya, Remote Sensing of Environment, 162, 55–66, https://doi.org/10.1016/j.rse.2015.01.031, 2015.

Dehecq, A., Gardner, A. S., Alexandrov, O., McMichael, S., Hugonnet, R., Shean, D., and Marty, M.: Automated Processing of Declassified KH-9 Hexagon Satellite Images for Global Elevation Change Analysis Since the 1970s, Front. Earth Sci., 8, https://doi.org/10.3389/feart.2020.566802, 2020.

Delaloye, R., Lambiel, C., and Gärtner-Roer, I.: Overview of rock glacier kinematics research in the Swiss Alps., Geogr. Helv., 135–145, 2010.

DGA: Dinámica de Glaciares Rocosos en el Chile Semiárido: Parte I, Plan de Monitoreo., 2010.

DGA: INVENTARIO PÚBLICO DE GLACIARES, actualización 2022. SDT N°447, 2022. Ministerio de Obras Públicas, Dirección General de Aguas Unidad de Glaciología y Nieves. Realizado por: Casassa, G., Espinoza, A., Segovia, A., Huenante, J., 2022.

Doin, M.-P., Guillaso, S., Jolivet, R., Lasserre, C., Lodge, F., Ducret, G., and Grandin, R.: Presentation of the small baseline NSBAS processing chain on a case example: The Etna deformation monitoring from 2003 to 2010 using Envisat data, in: Proceedings of the Fringe symposium, Citation Key: doin2011presentation, 3434–3437, 2011.

Etzelmüller, B., Guglielmin, M., Hauck, C., Hilbich, C., Hoelzle, M., Isaksen, K., Noetzli, J., Oliva, M., and Ramos, M.: Twenty years of European mountain permafrost dynamics—the PACE legacy, Environ. Res. Lett., 15, 104070, https://doi.org/10.1088/1748-9326/abae9d, 2020.

Facciolo, G., De Franchis, C., and Meinhardt, E.: MGM: A significantly more global matching for stereovision, in: BMVC 2015, 2015.

Garreaud, R. D., Boisier, J. P., Rondanelli, R., Montecinos, A., Sepúlveda, H. H., and Veloso-Aguila, D.: The central chile mega drought (2010–2018): A climate dynamics perspective, International Journal of Climatology, 40, 421–439, https://doi.org/10.1002/joc.6219, 2020.

Gärtner-Roer, I., Brunner, N., Delaloye, R., Haeberli, W., Kääb, A., and Thee, P.: Glacier-permafrost relations in a high-mountain environment: 5 decades of kinematic monitoring at the Gruben site, Swiss Alps, The Cryosphere Discussions, 1–30, https://doi.org/10.5194/tc-2021-208, 2021.

GCOS: Plan for the Global Climate Observing System, version 1.0., 1995.

Grandin, R.: Interferometric processing of SLC sentinel-1 TOPS data, in: FRINGE'15: Advances in the science and applications of SAR interferometry and sentinel-1 InSAR workshop, frascati, italy, 23-27 march 2015, Citation Key: grandin2015interferometric, 2015.

Gruber, S.: Derivation and analysis of a high-resolution estimate of global permafrost zonation, The Cryosphere, 6, 221–233, https://doi.org/10.5194/tc-6-221-2012, 2012.

Haberkorn, A., Kenner, R., Noetzli, J., and Phillips, M.: Changes in ground temperature and dynamics in mountain permafrost in the swiss alps, Frontiers in Earth Science, 9, https://doi.org/10.3389/feart.2021.626686, 2021.

Haeberli, W., Hallet, B., Arenson, L., Elconin, R., Humlum, O., Kääb, A., Kaufmann, V., Ladanyi, B., Matsuoka, N., Springman, S., and Mühll, D. V.: Permafrost creep and rock glacier dynamics, Permafrost and Periglacial Processes, 17, 189–214, https://doi.org/10.1002/ppp.561, 2006.

Haeberli, W., Schaub, Y., and Huggel, C.: Increasing risks related to landslides from degrading permafrost into new lakes in de-glaciating mountain ranges, Geomorphology, 293, 405–417, https://doi.org/10.1016/j.geomorph.2016.02.009, 2017.

Halla, C., Blöthe, J. H., Tapia Baldis, C., Trombotto Liaudat, D., Hilbich, C., Hauck, C., and Schrott, L.: Ice content and interannual water storage changes of an active rock glacier in the dry Andes of Argentina, The Cryosphere, 15, 1187–1213, https://doi.org/10.5194/tc-15-1187-2021, 2021.

Hartl, L., Fischer, A., Stocker-waldhuber, M., and Abermann, J.: Recent speed-up of an alpine rock glacier: an updated chronology of the kinematics of outer hochebenkar rock glacier based on geodetic measurements, Geografiska Annaler: Series A, Physical Geography, 98, 129–141, https://doi.org/10.1111/geoa.12127, 2016.

Hartl, L., Zieher, T., Bremer, M., Stocker-Waldhuber, M., Zahs, V., Höfle, B., Klug, C., and Cicoira, A.: Multi-sensor monitoring and data integration reveal cyclical destabilization of the Äußeres Hochebenkar rock glacier, Earth Surface Dynamics, 11, 117–147, https://doi.org/10.5194/esurf-11-117-2023, 2023.

Heid, T. and Kääb, A.: Evaluation of existing image matching methods for deriving glacier surface displacements globally from optical satellite imagery, Remote Sensing of Environment, 118, 339–355, https://doi.org/10.1016/j.rse.2011.11.024, 2012.

Hock, R., Rasul, G., Adler, C., Caceres, B., Gruber, S., Hirabayashi, Y., Jackson, M., Kääb, A., Kang, S., Kutuzov, S., Milner, Al., Molau, U., Morin, S., Orlove, B., and Steltzer, H.: High Mountain Areas. In: IPCC Special Report on the Ocean and Cryosphere in a Changing Climate [H.-O. Pörtner, D.C. Roberts, V. Masson-Delmotte, P. Zhai, M. Tignor, E. Poloczanska, K. Mintenbeck, A. Alegría, M. Nicolai, A. Okem, J. Petzold, B. Rama, N.M. Weyer (eds.)]., Cambridge University Press, Cambridge, 131–202, https://doi.org/10.1017/9781009157964.004., 2019.

Höhle, J. and Höhle, M.: Accuracy assessment of digital elevation models by means of robust statistical methods, ISPRS Journal of Photogrammetry and Remote Sensing, 64, 398–406, https://doi.org/10.1016/j.isprsjprs.2009.02.003, 2009.

Hu, Y., Harrison, S., Liu, L., and Wood, J. L.: Modelling rock glacier ice content based on InSAR-derived velocity, Khumbu and Lhotse valleys, Nepal, The Cryosphere, 17, 2305–2321, https://doi.org/10.5194/tc-17-2305-2023, 2023.

Hugonnet, R., McNabb, R., Berthier, E., Menounos, B., Nuth, C., Girod, L., Farinotti, D., Huss, M., Dussaillant, I., Brun, F., and Kääb, A.: Accelerated global glacier mass loss in the early twenty-first century, Nature, 592, 726–731, https://doi.org/10.1038/s41586-021-03436-z, 2021.

IANIGLA: Inventario Nacional de Glaciares 2018. Resumen ejecutivo de los resultados del Inventario Nacional de Glaciares. IANIGLA-CONICET, Ministerio de Ambiente y Desarrollo Sustentable de la Nacion. Pp. 27, 2018.

Janke, J. and Frauenfelder, R.: The relationship between rock glacier and contributing area parameters in the Front Range of Colorado, Journal of Quaternary Science, 23, 153–163, https://doi.org/10.1002/jqs.1133, 2008.

Janke, J., Bellisario, A., and Ferrando, F.: Classification of debris-covered glaciers and rock glaciers in the Andes of central Chile, Geomorphology, 241, https://doi.org/10.1016/j.geomorph.2015.03.034, 2015.

Jansen, F. and Hergarten, S.: Rock glacier dynamics: Stick-slip motion coupled to hydrology, Geophysical Research Letters, 33, https://doi.org/10.1029/2006GL026134, 2006.

Kääb, A., Frauenfelder, R., and Roer, I.: On the response of rockglacier creep to surface temperature increase, Global and Planetary Change, 56, 172–187, https://doi.org/10.1016/j.gloplacha.2006.07.005, 2007.

Kääb, A., Strozzi, T., Bolch, T., Caduff, R., Trefall, H., Stoffel, M., and Kokarev, A.: Inventory and changes of rock glacier creep speeds in Ile Alatau and Kungöy Ala-Too, northern Tien Shan, since the 1950s, The Cryosphere, 15, 927–949, https://doi.org/10.5194/tc-15-927-2021, 2021.

Kääb, A. and Røste, J.: Rock glaciers across the United States predominantly accelerate coincident with rise in air temperatures, Nat Commun, 15, 7581, https://doi.org/10.1038/s41467-024-52093-z, 2024.

Kalthoff, N., Bischoff-Gauß, I., Fiebig-Wittmaack, M., Fiedler, F., Thürauf, J., Novoa, E., Pizarro, C., Castillo, R., Gallardo, L., Rondanelli, R., and Kohler, M.: Mesoscale Wind Regimes in Chile at 30°S, Journal of Applied Meteorology and Climatology, 41, 953–970, https://doi.org/10.1175/1520-0450(2002)041<0953:MWRICA>2.0.CO;2, 2002.

Kaufmann, V., Kellerer-Pirklbauer, A., and Seier, G.: Conventional and UAV-Based Aerial Surveys for Long-Term Monitoring (1954–2020) of a Highly Active Rock Glacier in Austria, Frontiers in Remote Sensing, 2, 2021.

Kellerer-Pirklbauer, A. and Kaufmann, V.: About the relationship between rock glacier velocity and climate parameters in central Austria, Austrian Journal of Earth Sciences, 105, 94–112, 2012.

Kellerer-Pirklbauer, A., Lieb, G. K., and Kaufmann, V.: Rock Glaciers in the Austrian Alps: A General Overview with a Special Focus on Dösen Rock Glacier, Hohe Tauern Range, in: Landscapes and Landforms of Austria, edited by: Embleton-Hamann, C., Springer International Publishing, Cham, 393–406, https://doi.org/10.1007/978-3-030-92815-5_27, 2022.

Kellerer-Pirklbauer, A., Bodin, X., Delaloye, R., Lambiel, C., Gärtner-Roer, I., Bonnefoy-Demongeot, M., Carturan, L., Damm, B., Eulenstein, J., Fischer, A., Hartl, L., Ikeda, A., Kaufmann, V., Krainer, K., Matsuoka, N., Cella, U. M. D., Noetzli, J., Seppi, R., Scapozza, C., Schoeneich, P., Stocker-Waldhuber, M., Thibert, E., and Zumiani, M.: Acceleration and interannual variability of creep rates in mountain permafrost landforms (rock glacier velocities) in the European Alps in 1995–2022, Environmental Research Letters, 19, 034022, https://doi.org/10.1088/1748-9326/ad25a4, 2024.

Kenner, R., Phillips, M., Beutel, J., Hiller, M., Limpach, P., Pointner, E., and Volken, M.: Factors Controlling Velocity Variations at Short-Term, Seasonal and Multiyear Time Scales, Ritigraben Rock Glacier, Western Swiss Alps, Permafrost and Periglac. Process., 28, 675–684, https://doi.org/10.1002/ppp.1953, 2017.

Kenner, R., Pruessner, L., Beutel, J., Limpach, P., and Phillips, M.: Why rock glacier deformation velocities correlate with both ground temperatures and water supply at multiple temporal scales, , https://doi.org/10.5194/egusphere-egu2020-9534, 2020.

824 Kooistra, L., Berger, K., Brede, B., Graf, L. V., Aasen, H., Roujean, J.-L., Machwitz, M., Schlerf, M., Atzberger, C.,
825 Prikaziuk, E., Ganeva, D., Tomelleri, E., Croft, H., Reyes Muñoz, P., Garcia Millan, V., Darvishzadeh, R., Koren, G.,
826 Herrmann, I., Rozenstein, O., Belda, S., Rautiainen, M., Rune Karlsen, S., Figueira Silva, C., Cerasoli, S., Pierre, J., Tanır
827 Kayıkçı, E., Halabuk, A., Tunc Gormus, E., Fluit, F., Cai, Z., Kycko, M., Udelhoven, T., and Verrelst, J.: Reviews and
828 syntheses: Remotely sensed optical time series for monitoring vegetation productivity, Biogeosciences, 21, 473–511,
829 https://doi.org/10.5194/bg-21-473-2024, 2024.

830 Kunz, J. and Kneisel, C.: Glacier–Permafrost Interaction at a Thrust Moraine Complex in the Glacier Forefield Muragl,
831 Swiss Alps, Geosciences, 10, 205, https://doi.org/10.3390/geosciences10060205, 2020.

832 Lacroix, P., Araujo, G., Hollingsworth, J., and Taipe, E.: Self-Entrainment Motion of a Slow-Moving Landslide Inferred
833 From Landsat-8 Time Series, Journal of Geophysical Research: Earth Surface, 124, 1201–1216,
834 https://doi.org/10.1029/2018JF004920, 2019.

835 Lacroix, P., Dehecq, A., and Taipe, E.: Irrigation-triggered landslides in a Peruvian desert caused by modern intensive
836 farming, Nat. Geosci., 13, 56–60, https://doi.org/10.1038/s41561-019-0500-x, 2020a.

837 Lacroix, P., Handwerger, A. L., and Bièvre, G.: Life and death of slow-moving landslides, Nat Rev Earth Environ, 1, 404–
838 419, https://doi.org/10.1038/s43017-020-0072-8, 2020b.

839 Lacroix, P., Belart, J. M. C., Berthier, E., Sæmundsson, Þ., and Jónsdóttir, K.: Mechanisms of Landslide Destabilization
840 Induced by Glacier-Retreat on Tungnakvíslarjökull Area, Iceland, Geophysical Research Letters, 49, e2022GL098302,
841 https://doi.org/10.1029/2022GL098302, 2022.

842 Lehmann, B., Anderson, R. S., Bodin, X., Cusicanqui, D., Valla, P. G., and Carcaillet, J.: Alpine rock glacier activity over
843 Holocene to modern timescales (western French Alps), Earth Surface Dynamics Discussions, 1–40,
844 https://doi.org/10.5194/esurf-2022-8, 2022.

845 Lehmann, B., Anderson, R. S., Cusicanqui, D., Rossi, M. W., and Ochwat, N.: Exploring Holocene Climate History and
846 Alpine Landscape Evolution From Rock Glacier Dynamics: Mt Sopris, CO, USA, Journal of Geophysical Research: Earth
847 Surface, 130, e2024JF007978, https://doi.org/10.1029/2024JF007978, 2025.

848 Leprince, S., Berthier, E., Ayoub, F., Delacourt, C., and Avouac, J.-P.: Monitoring Earth Surface Dynamics With Optical
849 Imagery, Eos, Transactions American Geophysical Union, 89, 1–2, https://doi.org/10.1029/2008EO010001, 2008.

850 MacDonell, S., Farías, P. N., Aliste, V., Ayala, Á., Guzmán, C., Díaz, P. J., Schaffer, N., Schauwecker, S., Sproles, E. A.,
851 and Francisco, E. Y. S.: Snow and ice in the desert: reflections from a decade of connecting cryospheric science with
852 communities in the semiarid Chilean Andes, Annals of Glaciology, 63, 158–164, https://doi.org/10.1017/aog.2023.51, 2022.

Magnin, F., Ravanel, L., Bodin, X., Deline, P., Malet, E., Krysiecki, J.-M., and Schoeneich, P.: Main results of permafrost monitoring in the French Alps through the PermaFrance network over the period 2010–2022, Permafrost and Periglacial Processes, 35, 3–23, https://doi.org/10.1002/ppp.2209, 2024.

Manchado, A. M.-T., Allen, S., Cicoira, A., Wiesmann, S., Haller, R., and Stoffel, M.: 100 years of monitoring in the Swiss National Park reveals overall decreasing rock glacier velocities, Commun Earth Environ, 5, 1–17, https://doi.org/10.1038/s43247-024-01302-0, 2024.

Marcer, M., Cicoira, A., Cusicanqui, D., Bodin, X., Echelard, T., Obregon, R., and Schoeneich, P.: Rock glaciers throughout the French Alps accelerated and destabilised since 1990 as air temperatures increased, Commun Earth Environ, 2, 1–11, https://doi.org/10.1038/s43247-021-00150-6, 2021.

Markham, B. L., Storey, J. C., Williams, D. L., and Irons, J. R.: Landsat sensor performance: history and current status, IEEE Transactions on Geoscience and Remote Sensing, 42, 2691–2694, https://doi.org/10.1109/TGRS.2004.840720, 2004.

Masiokas, M. H., Villalba, R., Luckman, B. H., Quesne, C. L., and Aravena, J. C.: Snowpack Variations in the Central Andes of Argentina and Chile, 1951–2005: Large-Scale Atmospheric Influences and Implications for Water Resources in the Region, Journal of Climate, 19, 6334–6352, https://doi.org/10.1175/JCLI3969.1, 2006.

Masiokas, M. H., Villalba, R., Luckman, B. H., and Mauget, S.: Intra- to Multidecadal Variations of Snowpack and Streamflow Records in the Andes of Chile and Argentina between 30° and 37°S, Journal of Hydrometeorology, 11, 822–831, https://doi.org/10.1175/2010JHM1191.1, 2010.

Monnier, S. and Kinnard, C.: Reconsidering the glacier to rock glacier transformation problem: New insights from the central Andes of Chile, Geomorphology, 238, 47–55, https://doi.org/10.1016/j.geomorph.2015.02.025, 2015.

Monnier, S. and Kinnard, C.: Interrogating the time and processes of development of the Las Liebres rock glacier, central Chilean Andes, using a numerical flow model, Earth Surface Processes and Landforms, 41, 1884–1893, https://doi.org/10.1002/esp.3956, 2016.

Monnier, S. and Kinnard, C.: Internal structure and composition of a rock glacier in the Andes (upper Choapa valley, Chile) using borehole information and ground-penetrating radar, Annals of Glaciology, 54, 61–72, https://doi.org/10.3189/2013AoG64A107, 2013.

Monnier, S., Kinnard, C., Surazakov, A., and Bossy, W.: Geomorphology, internal structure, and successive development of a glacier foreland in the semiarid Chilean Andes (Cerro Tapado, upper Elqui Valley, 30 08′ S., 69 55′ W.), Geomorphology, 207, 126–140, 2014.

Montecinos, A. and Aceituno, P.: Seasonality of the ENSO-Related rainfall variability in central chile and associated circulation anomalies, Journal of Climate, 16, 281–296, https://doi.org/10.1175/1520-0442(2003)016<0281:SOTERR>2.0.CO;2, 2003.

Müller, J., Vieli, A., and Gärtner-Roer, I.: Rockglaciers on the run - Understanding rockglacier landform evolution and recent changes from numerical flow modeling, The Cryosphere Discussions, 1–40, https://doi.org/10.5194/tc-2016-35, 2016.

Navarro, G., MacDonell, S., and Valois, R.: A conceptual hydrological model of semiarid Andean headwater systems in Chile, Progress in Physical Geography: Earth and Environment, 47, 668–686, https://doi.org/10.1177/03091333221147649, 2023a.

Navarro, G., Valois, R., MacDonell, S., de Pasquale, G., and Díaz, J. P.: Internal structure and water routing of an ice-debris landform assemblage using multiple geophysical methods in the semiarid Andes, Frontiers in Earth Science, 11, https://doi.org/10.3389/feart.2023.1102620, 2023b.

Noetzli, J., Biskaborn, B. K., Christiansen, H. H., Isaksen, K., Schoeneich, P., Smith, P., Vieira, G., Zhao, L., and Streletskiy, D. A.: Permafrost thermal state. In Bull. Amer. Meteor. Soc. Vol. 100., in: State of Climate 2018, vol. 9, Bull. Amer. Meteor. Soc., 21–22, 2019.

Notarnicola, C.: Hotspots of snow cover changes in global mountain regions over 2000–2018, Remote Sensing of Environment, 243, 111781, https://doi.org/10.1016/j.rse.2020.111781, 2020.

Nuth, C. and Kääb, A.: Co-registration and bias corrections of satellite elevation data sets for quantifying glacier thickness change, The Cryosphere, 5, 271–290, https://doi.org/10.5194/tc-5-271-2011, 2011.

Obu, J.: How Much of the Earth's Surface is Underlain by Permafrost?, Journal of Geophysical Research: Earth Surface, 126, e2021JF006123, https://doi.org/10.1029/2021JF006123, 2021.

de Pasquale, G., Valois, R., Schaffer, N., and MacDonell, S.: Contrasting geophysical signatures of a relict and an intact Andean rock glacier, The Cryosphere, 16, 1579–1596, https://doi.org/10.5194/tc-16-1579-2022, 2022.

Patton, A. I., Rathburn, S. L., and Capps, D. M.: Landslide response to climate change in permafrost regions, Geomorphology, 340, 116–128, https://doi.org/10.1016/j.geomorph.2019.04.029, 2019.

Pei, Y., Qiu, H., Yang, D., Liu, Z., Ma, S., Li, J., Cao, M., and Wufuer, W.: Increasing landslide activity in the Taxkorgan River Basin (eastern Pamirs Plateau, China) driven by climate change, CATENA, 223, 106911, https://doi.org/10.1016/j.catena.2023.106911, 2023.

Pellet, C., Bodin, X., Cusicanqui, D., Delaloye, R., Kaab, A., Kaufmann, V., Noetzli, J., Thibert, E., Vivero, S., and Kellerer-Pirklbauer, A.: Rock glacier velocity, Bull. Amer. Meteor. Soc., 103, Si-S465, https://doi.org/10.1175/2022BAMSStateoftheClimate.1, 2022.

Poblete, A. G. and Minetti, J. L.: ¿Influye el calentamiento global en la disminución de las nevadas en los Andes Áridos?, Revista Universitaria de Geografía, 26, 11–29, 2017.

Réveillet, M., MacDonell, S., Gascoin, S., Kinnard, C., Lhermitte, S., and Schaffer, N.: Impact of forcing on sublimation simulations for a high mountain catchment in the semiarid Andes, The Cryosphere, 14, 147–163, https://doi.org/10.5194/tc-14-147-2020, 2020.

RGI Consortium: Randolph Glacier Inventory – A Dataset of Global Glacier Outlines: Version 6.0: Technical Report, Global Land Ice Measurements from Space., https://doi.org/10.7265/N5-RGI-60, 2017.

RGIK: Guidelines for inventorying rock glaciers, https://doi.org/10.51363/unifr.srr.2023.002, 2023.

Robson, B. A., MacDonell, S., Ayala, Á., Bolch, T., Nielsen, P. R., and Vivero, S.: Glacier and rock glacier changes since the 1950s in the La Laguna catchment, Chile, The Cryosphere, 16, 647–665, https://doi.org/10.5194/tc-16-647-2022, 2022.

Rosu, A.-M., Pierrot-Deseilligny, M., Delorme, A., Binet, R., and Klinger, Y.: Measurement of ground displacement from optical satellite image correlation using the free open-source software MicMac, ISPRS Journal of Photogrammetry and Remote Sensing, 100, 48–59, https://doi.org/10.1016/j.isprsjprs.2014.03.002, 2015.

Rupnik, E., Daakir, M., and Pierrot Deseilligny, M.: MicMac – a free, open-source solution for photogrammetry, Open Geospatial Data, Software and Standards, 2, 14, https://doi.org/10.1186/s40965-017-0027-2, 2017.

Schaffer, N. and MacDonell, S.: Brief communication: A framework to classify glaciers for water resource evaluation and management in the Southern Andes, The Cryosphere, 16, 1779–1791, https://doi.org/10.5194/tc-16-1779-2022, 2022.

Schaffer, N., MacDonell, S., Réveillet, M., Yáñez, E., and Valois, R.: Rock glaciers as a water resource in a changing climate in the semiarid Chilean Andes, Reg Environ Change, 19, 1263–1279, https://doi.org/10.1007/s10113-018-01459-3, 2019.

Schauwecker, S., Palma, G., MacDonell, S., Ayala, Á., and Viale, M.: The Snowline and 0°C Isotherm Altitudes During Precipitation Events in the Dry Subtropical Chilean Andes as Seen by Citizen Science, Surface Stations, and ERA5 Reanalysis Data, Front. Earth Sci., 10, https://doi.org/10.3389/feart.2022.875795, 2022.

Scherler, D., Leprince, S., and Strecker, M. R.: Glacier-surface velocities in alpine terrain from optical satellite imagery—Accuracy improvement and quality assessment, Remote Sensing of Environment, 112, 3806–3819, https://doi.org/10.1016/j.rse.2008.05.018, 2008.

Smith, M. J.: Chapter Eight - Digital Mapping: Visualisation, Interpretation and Quantification of Landforms, in: Developments in Earth Surface Processes, vol. 15, edited by: Smith, M. J., Paron, P., and Griffiths, J. S., Elsevier, 225–251, https://doi.org/10.1016/B978-0-444-53446-0.00008-2, 2011.

39

Sorg, A., Kääb, A., Roesch, A., Bigler, C., and Stoffel, M.: Contrasting responses of Central Asian rock glaciers to global warming, Scientific Reports, 5, 8228, https://doi.org/10.1038/srep08228, 2015.

Stammler, M., Cusicanqui, D., Bell, R., Robson, B., Bodin, X., Blöthe, J., and Schrott, L.: Vertical surface change signals of rock glaciers: combining UAV and Pléiades imagery (Agua Negra, Argentina), https://doi.org/10.52381/ICOP2024.138.1, 2024.

Strozzi, T., Caduff, R., Jones, N., Barboux, C., Delaloye, R., Bodin, X., Kääb, A., Mätzler, E., and Schrott, L.: Monitoring Rock Glacier Kinematics with Satellite Synthetic Aperture Radar, Remote Sensing, 12, 559, https://doi.org/10.3390/rs12030559, 2020.

Stumpf, A., Malet, J.-P., and Delacourt, C.: Correlation of satellite image time-series for the detection and monitoring of slow-moving landslides, Remote Sensing of Environment, 189, 40–55, https://doi.org/10.1016/j.rse.2016.11.007, 2017.

Sun, Z., Hu, Y., Racoviteanu, A., Liu, L., Harrison, S., Wang, X., Cai, J., Guo, X., He, Y., and Yuan, H.: TPRoGI: a comprehensive rock glacier inventory for the Tibetan Plateau using deep learning, Earth System Science Data Discussions, 1–32, https://doi.org/10.5194/essd-2024-28, 2024.

Thibert, E. and Bodin, X.: Changes in surface velocities over four decades on the Laurichard rock glacier (French Alps), Permafrost and Periglacial Processes, 33, 323–335, https://doi.org/10.1002/ppp.2159, 2022.

Thollard, F., Clesse, D., Doin, M.-P., Donadieu, J., Durand, P., Grandin, R., Lasserre, C., Laurent, C., Deschamps-Ostanciaux, E., Pathier, E., Pointal, E., Proy, C., and Specht, B.: FLATSIM: The ForM@Ter LArge-Scale Multi-Temporal Sentinel-1 InterferoMetry Service, Remote Sensing, 13, 3734, https://doi.org/10.3390/rs13183734, 2021.

Toth, C. and Jóźków, G.: Remote sensing platforms and sensors: A survey, ISPRS Journal of Photogrammetry and Remote Sensing, 115, 22–36, https://doi.org/10.1016/j.isprsjprs.2015.10.004, 2016.

Ustin, S. L. and Middleton, E. M.: Current and near-term advances in Earth observation for ecological applications, Ecological Processes, 10, 1, https://doi.org/10.1186/s13717-020-00255-4, 2021.

Villarroel, C., Tamburini Beliveau, G., Forte, A., Monserrat, O., Morvillo, M., Villarroel, C. D., Tamburini Beliveau, G., Forte, A. P., Monserrat, O., and Morvillo, M.: DInSAR for a Regional Inventory of Active Rock Glaciers in the Dry Andes Mountains of Argentina and Chile with Sentinel-1 Data, Remote Sensing, 10, 1588, https://doi.org/10.3390/rs10101588, 2018.

Vivero, S., Bodin, X., Farías-Barahona, D., MacDonell, S., Schaffer, N., Robson, B. A., and Lambiel, C.: Combination of aerial, satellite, and UAV photogrammetry for quantifying rock glacier kinematics in the dry andes of chile (30°S) since the 1950s, Frontiers in Remote Sensing, 2, https://doi.org/10.3389/frsen.2021.784015, 2021.

969 Wirz, V., Geertsema, M., Gruber, S., and Purves, R. S.: Temporal variability of diverse mountain permafrost slope
970 movements derived from multi-year daily GPS data, Mattertal, Switzerland, Landslides, 13, 67–83,
971 https://doi.org/10.1007/s10346-014-0544-3, 2016.

972 Wood, E., Bolch, T., and Streeter, R.: Insights from feature tracking of optical satellite data for studying rock glacier
973 kinematics in the Northern Tien Shan, Front. Earth Sci., 12, https://doi.org/10.3389/feart.2024.1518390, 2025.

974 Hu, Y., Arenson, L. U., Barboux, C., Bodin, X., Cicoira, A., Delaloye, R., Gärtner-Roer, I., Kääb, A., Kellerer-Pirklbauer,
975 A., Lambiel, C., Liu, L., Pellet, C., Rouyet, L., Schoeneich, P., Seier, G., and Strozzi, T.: Rock Glacier Velocity: An
976 Essential Climate Variable Quantity for Permafrost, Reviews of Geophysics, 63, e2024RG000847,
977 https://doi.org/10.1029/2024RG000847, 2025.